

# Confused sea-state induced fatigue

## N.C.H. Troost

Joint swell and wind seas induced multiaxial stresses: the influence of confused sea-state induced multiaxial stress-states on fatigue damage of a USCG cutter.



*Figure on cover by Quindit*

# Confused sea-state induced fatigue

by

N.C.H. Troost

to obtain the degree of Master of Science  
at the Delft University of Technology,  
to be defended publicly on December 14, 2017.

Student number:	4168321	
Project duration:	February 13, 2017 – December 14, 2017	
Date of defense:	December 14, 2017	
Master programma:	Master Offshore and Dredging Engineering	
Specialization:	Structural Analysis & Design	
Faculty:	Mechanical, Maritime and Materials Engineering	
Thesis committee:	Prof. dr. ir. M.L. Kaminski,	TU Delft, supervisor
	Prof. dr. ir. L.J. Sluys,	TU Delft
	Dr. ir. J.H. den Besten,	TU Delft
	Ir. P.S. van Lieshout,	TU Delft
	Ir. G. Bufalari,	TU Delft
	Ir. R.B. Hageman,	MARIN

*This thesis is confidential and cannot be made public until December 31, 2017.*

An electronic version of this thesis is available at <http://repository.tudelft.nl/>.





# Abstract

Marine structures are mostly exposed to mild and moderate sea-states, where the structural response is elastic. Characteristics of environmental loading are highly stochastic in nature, resulting in stress-states that might be multiaxial. This thesis attempts to identify the source and effect of these multiaxial stress-states on fatigue damage in frigate type structures.

A stress invariant based method called the Projection-by-Projection approach was adopted to estimate damage in the presence of multiaxial stress-states. This method was tested for its applicability and modified, where necessary, to better cope with the encountered stress-states. The design rules by the International Institute of Welding (IIW) were also used to be able to distinguish physical phenomena from methodological properties.

The available data consisted of strain measurements from the United States Coast Guard (USCG) Cutters Bertholf and Stratton. The Bertholf was equipped with the WaMoS wave radar. Measured wave data was reinforced with simulated waves to make the research independent of encountered sea-states.

It was concluded that multiaxiality is most relevant at low damage estimates (i.e.: low wave). The governing influence factor is the incoming wave direction. It was also shown that multiaxial stress-states may significantly contribute to fatigue damage (up to a factor 2, depending on the structural detail and location in the vessel) at an estimated life time of  $2 \cdot 10^6$  cycles.



# Preface

As a part of the fatigue Lifetime Assessment Project, I, in collaboration with MARIN and the Delft University of Technology, attempted to make sense of the complex loadings that are encountered while considering multi-axial stress-states in frigates. Most importantly, the effect of these multi-axial loadings on fatigue damage was investigated. This thesis has been written to obtain the long-awaited and much anticipated degree of Master of Science at the Delft University of Technology.

A special acknowledgment goes out to Remco Hageman. His input is much appreciated and valued; the realization of this thesis is due in part to his helping hand. I would also like to thank Henk den Besten for his knowledge, Paula van Lieshout for her helpfulness, Gabriele Bufalari for his insights and Mirek Kaminski, for providing me with this opportunity.

It is with great pleasure that I present to you this thesis. I hope it may bring you as much pleasure reading, as it brought me writing.

This is my contribution to material science.

*N.C.H. Troost  
Rotterdam, December 2017*



# Contents

<b>List of Figures</b>	<b>3</b>
<b>List of Tables</b>	<b>5</b>
<b>Nomenclature</b>	<b>7</b>
<b>1 Introduction</b>	<b>11</b>
1.1 Motivation . . . . .	11
1.1.1 Overview. . . . .	12
1.1.2 Problem statement. . . . .	12
1.2 Scope of work . . . . .	14
1.3 Outline . . . . .	15
<b>2 Theoretical framework</b>	<b>17</b>
2.1 General . . . . .	17
2.2 Fundamentals of fatigue . . . . .	17
2.3 Fatigue calculations. . . . .	19
2.3.1 Stress concepts. . . . .	19
2.3.2 Damage calculations. . . . .	20
2.3.3 Multiaxial fatigue . . . . .	21
<b>3 Projection-by-Projection approach</b>	<b>23</b>
3.1 General . . . . .	23
3.2 PbP implementation . . . . .	23
3.2.1 Mathematical properties. . . . .	23
3.2.2 Time-domain formulation of the PbP approach . . . . .	24
3.3 Applicability of the PbP approach. . . . .	27
3.3.1 Stress-state estimation. . . . .	27
3.3.2 Mean stress effect . . . . .	28
3.4 A modified approach . . . . .	29
3.4.1 General modifications . . . . .	29
3.4.2 Mean stress effect . . . . .	29
3.5 Validation. . . . .	31
3.5.1 Method of validation. . . . .	31
3.5.2 Results and discussion. . . . .	32
<b>4 Research methodology</b>	<b>35</b>
4.1 General . . . . .	35
4.2 Instrumentation and gathered environmental data . . . . .	35
4.3 Methods of research . . . . .	35
4.3.1 Model calculations. . . . .	35
4.3.2 Data post processing. . . . .	36
4.4 Data analysis . . . . .	37
4.4.1 General . . . . .	37
4.4.2 Environmental data . . . . .	37
4.4.3 Investigation of the effect of multiaxial stress-states on fatigue damage in frigate type structures . . . . .	39
<b>5 Results and discussion</b>	<b>43</b>
5.1 General . . . . .	43
5.2 Expected results. . . . .	43
5.2.1 Maximum response . . . . .	43
5.2.2 Proportionality. . . . .	44

---

5.3	Results . . . . .	44
5.3.1	Uniaxial vs. multiaxial damage. . . . .	44
5.3.2	Correlation with wave statistics . . . . .	48
5.4	Discussion . . . . .	51
<b>6</b>	<b>Conclusion and recommendation</b>	<b>55</b>
6.1	Conclusions. . . . .	55
6.2	Recommendation. . . . .	56
	<b>Bibliography</b>	<b>59</b>
<b>A</b>	<b>Characteristic equation, invariants and the definition of stress quantities</b>	<b>63</b>
<b>B</b>	<b>Wave characteristics</b>	<b>65</b>
<b>C</b>	<b>Structural stress method</b>	<b>67</b>
<b>D</b>	<b>Results</b>	<b>69</b>
<b>E</b>	<b>Validation of the Bertholf FE model</b>	<b>71</b>



# List of Figures

1.1	The USCG Cutter Bertholf. . . . .	11
1.2	Fatigue physics range of scales. . . . .	12
1.3	Structural response due to external loads. . . . .	13
1.4	Definition of load cases. . . . .	13
2.1	Example of a moving dislocation under cyclic shear loading. . . . .	18
2.2	mSC development at the material surface. . . . .	18
2.3	Fracture modes. . . . .	19
2.4	Weld toe notch stress components. . . . .	20
2.5	A typical double slope SN-curve . . . . .	21
3.1	Random load path in a 2-D space. . . . .	25
3.2	Master curves and reference curve. . . . .	25
3.3	Modified rainflow algorithm. . . . .	26
3.4	The reference parameter $\rho_{ref}$ for different loading conditions. . . . .	28
3.5	Reference SN-curves for different values of the stress-state estimator $\rho_{ref}$ . . . . .	28
3.6	SN-curves for different values of the mean stress. . . . .	29
3.7	Location of FSL04 and FSL05. . . . .	31
3.8	Top view detail of FSL04 and FSL05. . . . .	31
3.9	Damage estimates for filtered stress time histories at zero-mean hydrostatic stress. . . . .	32
3.10	Damage estimates for filtered stress time histories at fully compressive hydrostatic stress. . . . .	32
4.1	Location of FSL{01,02,03,04,05}. . . . .	36
4.2	Specification of FSL03. . . . .	37
4.3	Equal energy bins . . . . .	38
4.4	Spreading as a function of wave height. . . . .	39
4.5	Mean frequency as a function of wave height. . . . .	39
4.6	Specification of FSL01. . . . .	40
4.7	Specification of the reference location. . . . .	41
5.1	Maximum torsion in ships. . . . .	44
5.2	Transfer functions at a vessel speed of 15 <i>knots</i> . . . . .	45
5.3	Level of proportionality for the reference cold spot. . . . .	45
5.4	Level of proportionality for the reference HS. . . . .	45
5.5	Damage estimates from the USCG Cutter Stratton. . . . .	46
5.6	Uniaxial damage (in $N_f$ ) vs. multiaxial damage (in $N_f$ ) using analytical expressions. . . . .	47
5.7	Uniaxial damage (in $N_f$ ) vs. multiaxial damage (in $N_f$ ) for FSL01 (TF based). . . . .	47
5.8	Uniaxial damage (in $N_f$ ) vs. multiaxial damage (in $N_f$ ) for FSL04 and FSL05 (strain gauge based). . . . .	47
5.9	Uniaxial damage (in $N_f$ ) vs. multiaxial damage (in $N_f$ ) for the reference location using a cold spot approach (TF based). . . . .	47
5.10	Uniaxial damage (in $N_f$ ) vs. multiaxial damage (in $N_f$ ) for the reference location using a HS approach (TF based). . . . .	47
5.11	FSL01, uniaxial damage (in $N_f$ ) vs. wave height. . . . .	49
5.12	Reference location (HS approach), uniaxial damage (in $N_f$ ) vs. wave height. . . . .	49
5.13	FSL01, ratio $r$ vs. uniaxial damage (in $N_f$ ). . . . .	49
5.14	Reference location (HS approach), ratio $r$ vs. uniaxial damage (in $N_f$ ). . . . .	49
5.15	FSL01, correlation damage (in $N_f$ ) and wave height. . . . .	50
5.16	Reference location (HS approach), correlation damage (in $N_f$ ) and wave height. . . . .	50
5.17	FSL01, correlation damage (in $N_f$ ) and spreading. . . . .	50

5.18	Reference location (HS approach), correlation damage (in $N_f$ ) and spreading. . . . .	50
5.19	FSL01, correlation damage (in $N_f$ ) and the incoming peak wave direction. . . . .	50
5.20	Reference location (HS approach), correlation damage (in $N_f$ ) and the incoming peak wave direction. . . . .	50
5.21	Strain gauge data, correlation damage (in $N_f$ ) and wave height. . . . .	51
5.22	Strain gauge data, correlation damage (in $N_f$ ) and spreading. . . . .	51
5.23	Strain gauge data, correlation damage (in $N_f$ ) and the incoming peak wave direction. . . . .	51
5.24	Maximum damage obtained for a discrete set of wave heights as a function of spreading and incoming wave direction. . . . .	53
5.25	Maximum ratio $r$ obtained for a discrete set of wave heights as a function of spreading and incoming wave direction. . . . .	53
5.26	Maximum ratio $r$ . . . . .	53
5.27	Ratio $r$ in wave characteristics that result in the highest damage estimates. . . . .	53
B.1	A typical 3-D wave spectrum. . . . .	65
B.2	Energy per wave direction $E_\theta(\theta)$ . . . . .	65
B.3	Behavior of the spreading parameter for wave spreading modeled by two different wave spreading functions. . . . .	66
C.1	Specification of the FE model. . . . .	68
D.1	Uniaxial damage (per cycle) vs. multiaxial damage (per cycle) for FSL01 (TF based). . . . .	69
D.2	Uniaxial damage (per cycle) vs. multiaxial damage (per cycle) for FSL04 and FSL05 (strain gauge based). . . . .	69
D.3	Uniaxial damage (per cycle) vs. multiaxial damage (per cycle) for the reference location using a cold spot approach (TF based). . . . .	69
D.4	Uniaxial damage (per cycle) vs. multiaxial (per cycle) damage for the reference location using a hot spot approach (TF based). . . . .	69

# List of Tables

3.1	Damage estimates by the PbP approach for various load conditions. . . . .	28
4.1	Data on strain measurements. . . . .	36
4.2	Specifications wave radar system. . . . .	37
4.3	Summary of modeled waves. . . . .	39
4.4	Summary of the investigated data. . . . .	40
E.1	Sets of spectral moments for FE model validation. . . . .	72



# Nomenclature

## Abbreviations

<b>AP</b>	Anti-Phase
<b>BEM</b>	Boundary Element Method
<b>CA</b>	Constant Amplitude
<b>CoV</b>	Coëfficient of Variation
<b>FE</b>	Finite Element
<b>FEM</b>	Finite Element Method
<b>FFT</b>	Fast Fourier Transform
<b>FLAP</b>	Fatigue Lifetime Assessment Plan
<b>FSL</b>	Fatigue Sensitive Location
<b>HCF</b>	High Cycle Fatigue
<b>HS</b>	Hot Spot
<b>IIW</b>	International Institute of Welding
<b>IP</b>	In-Phase
<b>JIP</b>	Joint Industry Project
<b>LC</b>	Load Case
<b>MCF</b>	Medium Cycle Fatigue
<b>MSC</b>	Macroscopic Stress Concentration
<b>mSC</b>	Microscopic Stress Concentration
<b>NSC</b>	National Security Cutter
<b>OP</b>	Out-of-Phase
<b>PbP</b>	Projection-by-Projection
<b>PSB</b>	Persistent Slip Band
<b>RMS</b>	Root Mean Square
<b>SG</b>	Strain Gauge
<b>SIF</b>	Stress Intensity Factor
<b>SSD</b>	Spectral Statistical Difference
<b>TF</b>	Transfer Function
<b>USCG</b>	United States Coast Guard
<b>VA</b>	Variable Amplitude

## Latin symbols

$a$  Half crack length

$C$  Fatigue strength

**CV** Comparison Value in IIW design rules

$D$  Damage fraction

$D_m$  Specified Miner sum

$d_r$  Distance from notch tip

$E_\theta$  Spectral wave energy density as a function of wave direction

$g$  Gravitational acceleration

$H_s$  Significant wave height

$\sqrt{J_{2a}}$  Second invariant expressed by the deviatoric component of the Cauchy stress tensor

$k$  Slope in SN-curve

$K$  Stress intensity factor

$N_A$  Number of cycles to failure at knee point stress range

$N_f$  Number of cycles to failure

$P$  Remote loading in  $K$

$q$  Ratio mean hydrostatic stress over ultimate strength

$r$  Ratio uniaxial number of cycles to failure over multiaxial number of cycles to failure

$r_l$  Load ratio

$S$  Stress range

$S_d$  Design stress range

$S_L$  Stress range at knee point

$S_m$  Mean stress

$T$  Wave period

$T_p$  Peak period

$s$  The vector whose length equals the second invariant of the Cauchy stress tensor

## Greek symbols

$\alpha$  Mean stress correction function

$\beta$  Dimensionless material factor in  $\alpha$

$\gamma$  Defines the relative influence of the amplitude and mean stress in the Walker correction

$\lambda$  Wave length

$\Omega$  Load path

$\rho_{ref}$  Stress-state estimator in Projection-by-Projection approach

$\sigma_{ij}$  Stress component on plane  $i$  in direction  $j$



$\sigma_H$  Hydrostatic stress

$\sigma_R$  Fatigue resistance for normal loading

$\sigma_{xx}$  Longitudinal loading

$\sigma_{yy}$  Transverse loading

$\tau_R$  Fatigue resistance for shear loading

$\theta_I$  Incoming peak wave direction

$\theta_{spr}$  Wave spreading

$\tau_{xy}$  Shear loading

$\zeta$  Geometry factor in  $K$



# Introduction

*"And now for something completely different" –  
Monty Python*

---

## 1.1. Motivation

National Security Cutters (NSC) are the largest of several design of new United States Coast Guard (USCG) Cutters. The NSCs are the second longest of all USCG Cutters behind the research icebreaker Healy. One of these new NSCs is the USCG Cutter Bertholf.

The USCG set up a project to evaluate fatigue design approaches for these NSCs. This project became known as the Fatigue Lifetime Assessment Project (FLAP). MARIN, amongst other subject matter experts and stakeholders, was contracted to assist in this project and named it the VALID Joint Industry Project (JIP). The VALID JIP entails (from [3, 4]):

- Forecast structural maintenance needs of USCG Cutters.
- Improve understanding of wave loading induced fatigue.
- Increase confidence level in wave loading induced fatigue on a naval frigate type hull.

The data collected in the VALID JIP will be used to improve the design and maintenance needs using reliability based approaches in the VALID 2 JIP. The VALID 2 JIP is focused on the optimization of the service life maintenance sustainment efforts based on data obtained from a hull structure monitoring system.

The VALID JIP was initiated by and brought to the TU Delft by prof.dr.ir. M.L. Kaminski, former employee at MARIN, currently professor of Ship Hydromechanics and Structures at the TU Delft. Now, Ingo Drummen has the lead on the VALID JIP.



Figure 1.1: The USCG Cutter Bertholf (figure from [40]).

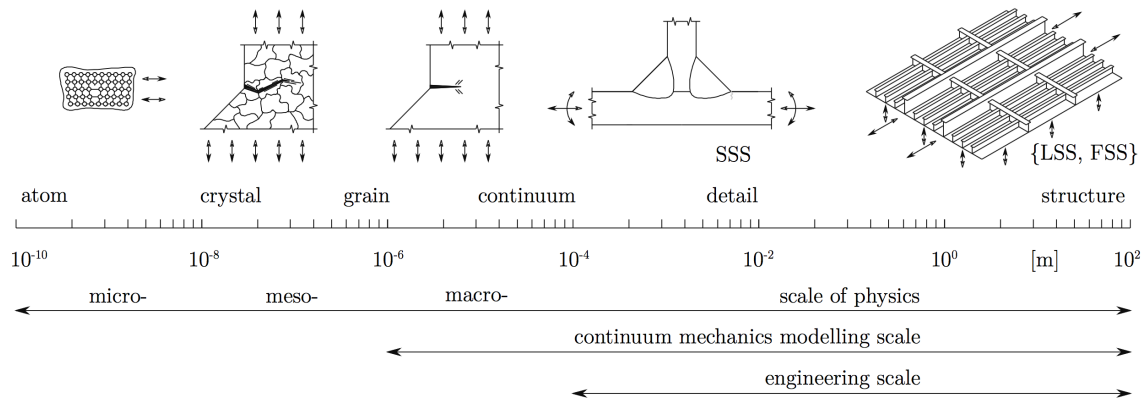


Figure 1.2: Fatigue physics range of scales (figure from [13]).

### 1.1.1. Overview

Marine structures are exposed to harsh environments. They are built to endure extreme events that are highly stochastic in nature. Offshore structures are also subjected to thousands and thousands of cycles of low amplitude loads. The cycle-by-cycle accumulation of damage due to low amplitude cyclic stresses is known as fatigue. The fatigue range of scales is depicted in Figure 1.2. The fatigue life is typically divided into two periods: the crack initiation period and the crack growth period. Crack initiation is a consequence of cyclic slip: moving dislocations as a result of a cyclic shear stress. The shear stress magnitude differs from grain to grain, depending on, amongst other influence factors, the orientation of the crystal structure. Crystal structures with an orientation that aligns with the maximum shear direction are most likely to form cyclic slip induced persistent slip bands (PSB). Due to the reduced constraint on slip, PSBs are preferably formed at the material surface. As microcracks - induced by stress concentrations due to slip bands - grow into the material, the constraint on slip increases; it becomes increasingly difficult to accommodate microcrack growth along slip bands. There is a tendency for the microcrack to deviate from its original path and grow perpendicular to the principal loading direction. Barriers for crack growth exist in the form of grain boundaries. As soon as the number of grains along the crack front becomes sufficiently large, crack growth occurs as a more or less continuous process. Surface effects such as surface roughness and reduced constraint on slip no longer affect the microcrack growth: it has entered the crack growth period. Fatigue of structures and materials is described in detail in [43]. Offshore structures are mainly subjected to high cycle fatigue (HCF), i.e.  $N = O(10^6 \dots 10^9)$ , in which crack growth dominates the fatigue lifetime.

The hull is predominantly loaded by hydrostatic forces (still water pressure), hydrodynamic forces (wave induced pressures) and cargo loads. The loads result in global bending moments and local bending moments which result in membrane stresses in the thin-walled plate structural members, and local pressures which result in bending stresses in structural members, as shown in Figure 1.3. Fatigue is governing in welded joints connecting hull girder structural members. Welded joints introduce notches and therefore stress concentrations, which makes the formation of PSBs immaterial.

### 1.1.2. Problem statement

#### *Multiaxial fatigue*

A previous study on fatigue performance under multiaxial loading in vessels was performed in [55] by Karl A. Stambaugh. The objective of this study was to survey and review methodologies for predicting multiaxial fatigue performance of structural details typical for marine structures. Multiaxial stresses can be in-phase (IP) or out-of-phase (OP) (Figure 1.4). A common type of a multiaxial stress state is a result of geometrical constraints: sudden changes in geometry such as notches or welds may result in uniaxial loading induced multiaxial stresses. Another type of a multiaxial stress state is due to externally applied multiaxial loading. The former type is proportional, meaning that stress components vary proportionally and principal stress directions remain unchanged. The latter is often non-proportional in nature. Karl Stambaugh at the time was limited by available models and methods. Moreover, the report is mainly focused on the effect of multiaxial stresses, rather than the loading components that create these stresses.

Multiaxial fatigue is a well-developed concept in the aerospace and automotive industries. Geometrical

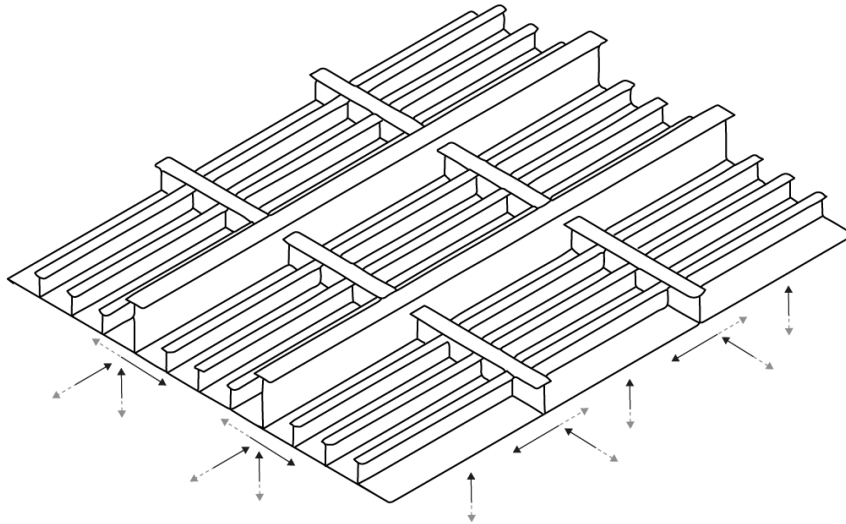


Figure 1.3: Structural response due to external loads.

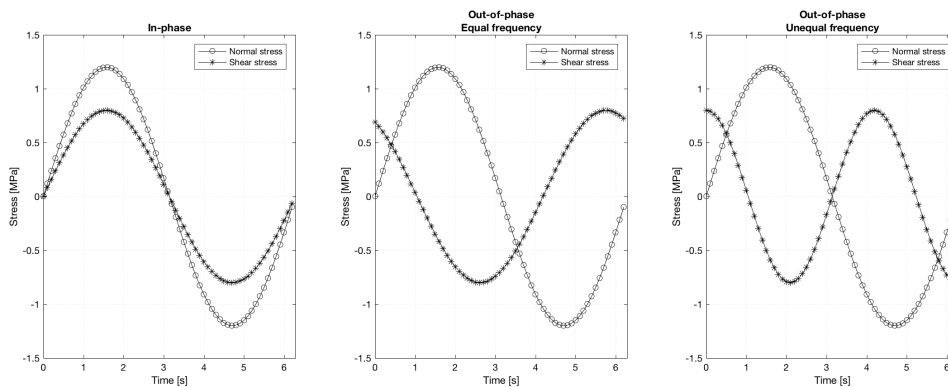


Figure 1.4: Definition of load cases. IP multiaxial stress, OP multiaxial stress with equal frequency and unequal frequency.

effects have a large influence on fatigue resistance and damage which makes scaling to marine structures difficult. The concept of multiaxial fatigue has been studied extensively; a brief overview is given in [45]. Previous research, among others, is performed in [10, 18, 29, 30] on path-dependent and -independent parameters, proportional and non-proportional constant amplitude (CA) and variable amplitude (VA) loading. The scope of this thesis retains the necessity to review these articles in detail. Underlying theory of multiaxial fatigue will be discussed in Chapter 2.

Methods to assess fatigue damage can be subdivided into three categories: stress, strain and energy based methods. Stress and strain based methods consider local components to calculate linear elastic stress (stress based method) or elastic-plastic strain (strain based method) histories. Fatigue cycles are generally extracted using the Rainflow counting algorithm; the damage per fatigue cycle can be calculated using the SN- (stress based) or EN-curve (strain based). The accumulation of damages per fatigue cycle can be assessed using, for example, Miner's rule. Energy based methods consider the internal energy balance to assess fatigue damage. The internal energy is elastically stored energy. Internal energy is dissipated, amongst other characteristics, when new free surface is created or in the formation of persistent slip bands.

### Structural response

Accurate prediction of the hydrodynamic loads on vessels is crucial to assess the structural stresses. Hydrodynamic loads can quite easily be calculated using potential theory. If the elastic deformation cannot be

neglected when compared to that induced by rigid-body motion, a hydroelastic approach is needed to assess the structural response. The first 2-D frequency domain hydroelastic method was proposed by [42]. In this method, the vessel was represented by a 2-D Timoshenko beam and the flow around the ship was determined using strip theory. The theory was developed to 3-D in [59] and extended to time domain in, among others, [58]. Nowadays, hydroelastic methods are used in 3-D full structure FEM and BEM, in frequency and time domain. When elastic deformation can be neglected when compared to the rigid-body motion, the hydrostructural (or rigid-body) approach will be accurate enough. An additional benefit of this hydrostructural approach over the hydroelastic approach is that it does not over complicate the model; including hydroelastic effects may induce results clouded with too many parameters that should not yet be considered.

### *Spectral analysis of stresses in ships*

A study was performed on the validation of naval vessel spectral fatigue analysis in [49]. Full-scale measurements were used to validate the spectral analysis. As an additional scope, the report looks at the influence of the chosen wave spectrum on the result. The research was based on a naval vessel that is heavier than the USCG Cutter Bertholf. Moreover, the research excluded springing and whipping and was focused on uniaxial, longitudinal stresses in cold spots. Local effects in hot spots may induce additional uncertainties, this makes the research fundamentally different from the research performed in this thesis. However, conclusions may prove useful: if uniaxial stresses can be predicted using a spectral analysis, multiaxial stresses might too. The results presented here are the root mean square (RMS) of the spectrum averaged over all strain gauges, coefficient of variation (CoV) averaged over all gauges and the damage estimates.

The RMS stress calculated using a 2-D spectrum on average differed by a factor 0.98 from the measured data with an (average) CoV of 0.25. For the 1-D spectrum this was respectively 1.35 and 0.46. For the damage estimates, the 2-D spectrum calculated RMS differed by a factor of 0.89 on average with an average CoV of 0.97. The 1-D results show 1.67 (RMS) and 1.47 (CoV). According to [49], linear frequency-domain hydrodynamic load spectra parameters and damage estimates were in good agreement with values derived from measurements. Parameters that introduce uncertainty are nonlinear behavior in hydrodynamics and structural response, operational profile and seaway representation. The results suggest a better representation of the seaway improves the spectral fatigue analysis. The poorest results for stress and damage were consistently with gauge s15 which was placed near the bow (the second poorest was s20, also near the bow). Stresses near the bow were less than half those of the remaining strain gauges. It was believed that the poorer performance of gauges near the bow was partly due to absolute errors in measurements and calculations causing more relative error at low strain measurements.

It should be noted that the validity of the results is extremely dependent of the encountered sea-states. The 1-D spectral results may provide sufficiently accurate results, if the encountered sea state was by approximation 1-dimensional. Insufficient data was collected to draw valuable conclusions to this respect.

## **1.2. Scope of work**

Fatigue design is mostly based on uniaxial Mode-I induced tensile loading; multiaxial fatigue regulations are in development ([7]) Potentially, this could be a non-conservative approach and may lead to significant underestimations of fatigue damage. This thesis aims to provide insight in the source and effect of multiaxial stresses and fatigue in vessels, in particular in the USCG Cutter Bertholf.

The research will be limited to a linear, frequency domain hydrostructural study on the correlation between the level of stress state multiaxiality and joint swell and wind waves. Non-linear time domain analysis may be performed later for validatory reasons but are deemed unnecessarily time-consuming and complex for the initial analysis. Measured wave data will be used to assess fatigue damage. The objectives are:

- To investigate the effect of multiaxial stress-states on fatigue damage in frigate type structures.
- To test the applicability of a model to estimate multiaxial fatigue damage - the Projection-by-Projection (PbP) approach - when applied to welded joints in a frigate type structure.

The research question is:

*Do multiaxial stress-states in ships result in significantly higher fatigue damage than uniaxial stress-states?*



### 1.3. Outline

In Chapter 2 fundamentals about fatigue and fracture are explained. It describes the fatigue crack initiation and growth mechanism, how fatigue life is generally calculated and why multiaxial fatigue is different from uniaxial fatigue. Chapter 3 explains and discusses the employed model to estimate fatigue damage. It will include a detailed description of the method and comprehensive investigation of its applicability on welded components in frigate type structures. How the influence of multiaxial stress-states is investigated, is discussed in Chapter 4. This chapter will include all employed concepts, as well as elaborate on the instrumentation of the USCG Cutter Bertholf and environmental data. The results are depicted and discussed in Chapter 5. Conclusions and recommendations are included in Chapter 6.

Text in boxes is sometimes included in this thesis as extra information. These pieces of text may increase the level of understanding of the reader, even if it does not necessarily provide new information.



# 2

## Theoretical framework

*"If you want to find the secrets of the Universe,  
think in terms of energy, frequency, and  
vibration"* – Nicola Tesla

---

### 2.1. General

Fatigue limit state design is important since the most encountered environmental conditions - mild and moderate - contribute to fatigue damage. Fatigue in materials starts at the microscale: atom dislocations in the crystal structure of a material may result in fracture of structural members. The mechanism of fatigue and fracture, and how it translates to the macroscale, is treated in this chapter.

### 2.2. Fundamentals of fatigue

Fatigue is typically divided in two periods: crack initiation and crack growth. In marine structures, materials consist of grains in a polycrystalline structure, of which the size is in the order of tens of micrometers. The atoms in a grain are oriented in a particular direction, making them microscopically anisotropic. The random orientation of all grains together makes the material macroscopically isotropic. This anisotropic behavior results in micro- and mesoscopic stress concentrations (mSC) at grain boundaries.

Another source of microscopic stress concentrations is crystal structure defects [13, 43]. At the formation of a polycrystalline structure, misplaced atoms such as in Figure 2.1 (most left illustration) will always occur. Defects exist as point, line and surface defects; the location and number in base material is completely random. Crystal dislocation start to move under cyclic loading, following the path of least resistance (Figure 2.1). This process is called cyclic slip. It appears that these dislocations move along slip planes under local cyclic shear, principally until the grain boundary is reached, causing micro-plastic deformation that typically concentrate in slip bands.

A favorable grain orientation for slip band formation exists: the grain orientation that aligns with the maximum shear stress. It can easily be verified using Mohr's circle [16] that this orientation is at an angle of  $\pm 45^\circ$  for normal loading, and  $\{0, 90\}^\circ$  for torsional loading. At the material surface, there are no neighboring grains to constrain plastic deformation. As a result, a preferred location for the development slip bands is at the material surface. A very practical argument that also supports slip band formation at the material surface is the presence of notches. A peak stress occurs near the surface facilitating easier slip band development. In conclusion: crack initiation is a near surface phenomenon.

When a moving dislocation reaches the material surface, much like it reaches the grain boundary in Figure 2.1, a notch is created. The next half cycle will create an intrusion (or extrusion). This mechanism is depicted in Figure 2.2. The accumulation of dislocations at the material surface causes surface roughening in the form of extrusion and intrusions [38]. microcracks start to grow along PSBs due to mSCs at extreme intrusions.

Other sources of mSCs that facilitate microcrack growth are corrosion pits, manufacturing defects or inclusions such as voids and pores [43]. Such manufacturing defects and inclusions are always present at welds.

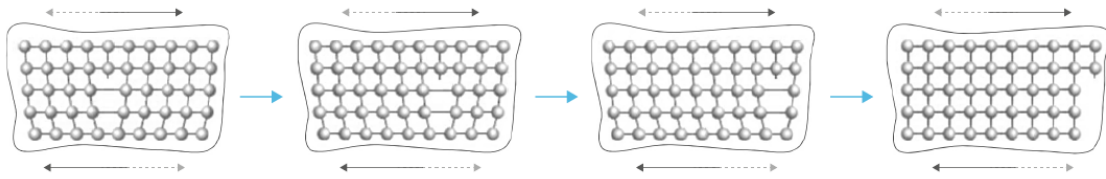


Figure 2.1: Example of a moving dislocation under cyclic shear loading (figure based on [13]).

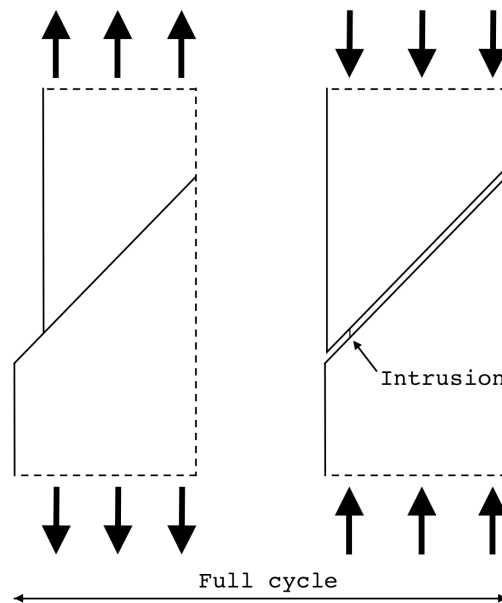


Figure 2.2: mSC development at the material surface.

This omits the necessity for mSC development due to cyclic slip if a weld is considered; crack initiation can occur underneath the surface. For this reason, welds are often considered governing in fatigue lifetime [43]. Additionally, welds will often coincide with a change in geometry, resulting in macroscopic stress concentrations (MSC). When the (micro-) crack tip reaches a grain boundary, mSC will result in further growth along PSBs or along grain boundaries. When the crack tip reaches deeper into the material, the added constraint on cyclic slip makes it harder to facilitate crack growth along PSBs. By this time, the crack front will cross multiple grains (multiple active PSBs). There is a tendency for the crack growth direction to deviate from its original path (maximum shear plane) to perpendicular to the principal loading direction. Surface effect no longer affect the crack growth; it has become a far-field stress dependent process. The crack initiation period is considered to be completed, crack growth is no longer a surface phenomenon but a bulk material property.

In fracture mechanics, there are three ways of applying a force that results in crack propagation [44]:

- Mode I: opening mode.
- Mode II: In-plane shearing.
- Mode III: Out-of-plane shearing.

These three modes are depicted in Figure 2.3. A crack tip can be considered a notch with an infinitely small radius. Explicit functions for the stress distribution around the crack tip can be obtained by considering the analytic limits for a short distance of a point  $((x, y)$  to the crack tip. These functions can be written as [24, 39]:

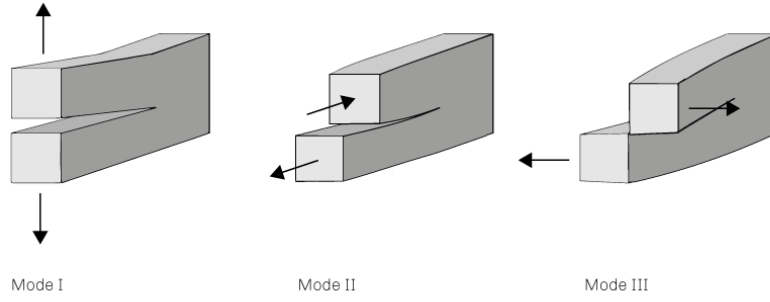


Figure 2.3: Fracture modes (figure based on [2]).

$$\sigma_{ij} = \frac{K}{\sqrt{2\pi d_r}} f_{i,j}(\theta) \quad (2.1)$$

with

$$K = \zeta P \sqrt{\pi a} \quad (2.2)$$

where the indices  $i$  and  $j$  represent the different stress components in the Cauchy stress tensor. This function was derived for an infinite sheet in [43],  $\zeta$  is a geometry factor that accounts for finite dimensions and other geometries in the stress intensity factor (SIF)  $K$ . The parameters  $d_r$ ,  $a$  and  $P$  respectively represent the distance from the crack tip, half the crack length and the remote loading. It is important to note that these equations apply to a mode I crack. It can be argued that, assuming mode I crack growth is dominant, a critical plane approach can be adopted to apply the same equations in the presence of shear loading. All stress components go to infinity for  $r \rightarrow 0$ . As a result of ductility, a small plastic zone will be created at the crack tip. The size and shape of the plastic zone depend on the stress-state (plane stress or plane strain). This is treated in [11, 37]

A cyclic load introduces a cyclic SIF varying between  $K_{max}$  and  $K_{min}$ . A cycle can be fully described using the following two definitions:

$$\Delta K = K_{max} - K_{min} \quad (2.3)$$

$$r_l = \frac{K_{min}}{K_{max}} \quad (2.4)$$

where  $r_l$  is known as the load ratio. According to [43], it appears to be fully correct that the crack growth rate (crack growth per cycle) is a function of  $\Delta K$  and  $r_l$ :

$$\frac{da}{dN} = f(\Delta K, r_l) \quad (2.5)$$

## 2.3. Fatigue calculations

### 2.3.1. Stress concepts

For the assessment of fatigue damage, one typically utilizes a nominal, structural (hot spot) or effective notch stress concept [7, 17]. The concepts take progressively more information about the weld in consideration, which makes the computation more complex, but more accurate as well. The total weld toe notch stress can be described by the superposition of the equilibrium-equivalent stress and self-equilibrating stress (Figure 2.4). The nominal stress concept is a global structural response approach. This concept takes no weld information or geometry changes into account; it only utilizes the equilibrium-equivalent stress. The structural (hot spot) stress concept is a local approach; this approach takes local structural (i.e.: geometry) variations (V-shaped notch stress) into account. Notch angle effects are excluded; theoretically, the fatigue strength is undefinable because the it grows with the notch radius. The effective notch stress concept takes the weld-load carrying stress into account (notch angle effects). This concept takes into account all global and local information; theoretically, one fatigue resistance curve with one reference radius (for weld toe and weld root notches) exists. Limitations exist in the form of elastoplastic behavior, which has to be taken into account

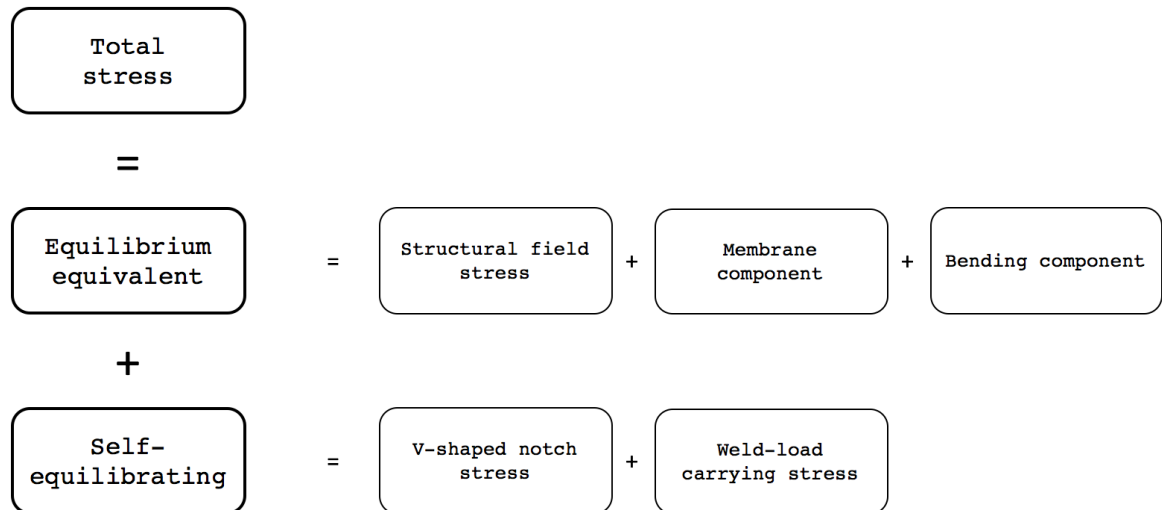


Figure 2.4: Weld toe notch stress components.

explicitly. If applied, cross-sectional weakening and strengthening must also be taken into account explicitly. A nominal stress concept requires resistance data specific to a particular detail. This means it cannot be used for unusual details. The effective notch stress concept requires detail specific information such as weld thickness. More importantly, multiaxial fatigue methods have not developed far enough to utilize this concept. A structural (hot spot) stress concept was adopted in this thesis.

### 2.3.2. Damage calculations

Fatigue damage calculations can be performed in time domain and frequency domain. In frequency domain, the damage is related to power spectral density information of the stress components. This approach is valid when the response is by approximation linear. When the response is expected to be non-linear, a time domain approach must be adopted. Time domain approaches estimate fatigue damage from stress time histories. The type of model also depends on the type of material; the behavior of a structure depends on the ductility of the material.

HCF is dominated by the crack initiation period [14]. The structural response is elastic [46]; fatigue life-time can be estimated using a linear stress-strain relationship. It is assumed that the geometry is intact for the largest part of its lifetime. LCF is dominated by the crack growth period. The structural response can be characterized by elastic-plastic deformation, which cannot be assessed using a linear stress-strain relationship. The crack growth is often estimated using fracture mechanics. Fracture mechanics is in detail treated in [44].

Marine structures are typically loaded in the HCF region. Fatigue damage can be estimated using either stress (or strain, since the response is linear) or energy relations. Energy concepts assume that the fatigue lifetime can be estimated by considering the energy dissipation in time. Fatigue calculations from stress time histories are performed using SN-curves. On an SN-curve, the amount of cycles to failure is plotted as a function of the stress range in a Wöhler diagram. Note that, even though the stress range is the parameter that can be influenced in a fatigue test, it is plotted on the Y-axis. SN-curves are obtained from test data. For fatigue calculations, SN-curves are often modeled using single slope or double slope models, with a knee point typically at  $2 \cdot 10^6$  cycles [7]. In double slope models, the change in damage mechanism (slope in the SN-curve) that appears at a certain amount of cycles (the knee point) is included. FAT classes define the resistance parameters for structural details. A FAT 71 SN-curve, defined in [7], is depicted in Figure 2.5. The formula for a single slope model is:

$$\log N_f = \log C - k \cdot \log S \quad (2.6)$$

where  $N_f$  is the number of cycles to failure,  $S$  the stress range,  $C$  the fatigue strength and  $k$  the slope in the SN-curve.

A Rainflow algorithm is used to extract cycles from a stress time history. This algorithm was first described



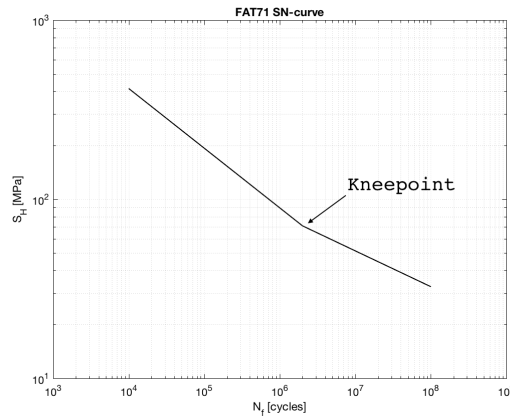


Figure 2.5: A typical double slope SN-curve

in [21]. The Rainflow algorithm, using the stress time history as input, returns the amplitude of all cycles it finds. The SN curve is used to determine the damage done per cycle. Damage may be assumed to be a linear or non-linear sum of the damage per cycle. For example: the damage sum is assumed non-linear when it is taken into account that the ductility of a material changes in the process of fatigue damage.

A recommended practice for the fatigue design of offshore steel structures is provided by DNV-GL in [17].

### 2.3.3. Multiaxial fatigue

Multiaxial fatigue is even more complex in that different stress components have different failure mechanisms (different slopes in the SN-curve). If no interaction between the damage mechanisms is taken into account, a linear damage sum may be applicable. For multiaxial fatigue, this is not a fair assumption:

Imagine a purely torsional CA far-field loading. If the loading plane is rotated  $45^\circ$  (using Mohr's circle), it is obvious from a physical point of view that the damage estimate should remain the same. The rotated plane has a normal stress on both the  $x$ - and  $y$ -plane in anti-phase (AP), with the same amplitude as the torsional loading. Assuming that normal loading results in higher damage than torsional loading (which often is a valid assumption), the sum of the damage on the rotated plane (due to longitudinal and transverse normal loading) will be much higher than the damage on the original plane (due to torsional loading).

A fatigue resistance parameter can be defined by the Cauchy stress tensor on a predefined plane or a critical plane [48], by an invariant of the Cauchy stress tensor [52] or by energy criteria [28]. A distinguish is made between methods that assume separate mode SN-curves and mixed mode SN-curves. Separate mode approaches use separate SN-curves for different stress components, mixed mode approaches attempt to define one SN-curve to estimate damage done by different stress components (or components of some invariant). A separate mode approach can be found in [7]. This method, developed by the International Institute of Welding (IIW), takes into account ductility, load characteristics (CA and VA loading), load proportionality and mean stress fluctuations. The method utilizes two parameters,  $D_m$  and  $CV$ , that allow for corrections based on the named influence factors. The design resistance is defined by FAT class. The IIW design rules define a design amplitude as:

$$S_d = \sqrt[m_1]{\frac{1}{D_m} \cdot \frac{\sum S_1^{m_1} + S_L^{m_1-m_2} \cdot \sum S_2^{m_2}}{\sum n_1 + \sum n_2}} \quad (2.7)$$

where

- $D_m$ : specified Miner Sum.
- $N_A$ : number of cycles to failure at knee point stress range.
- $m_1$ : slope above knee point.
- $m_2$ : slope below knee point.

- $S_1$ : stress range (counted using a Rainflow algorithm) above knee point.
- $S_2$ : stress range (counted using a Rainflow algorithm) below knee point.
- $S_L$ : stress range at knee point.
- $n_i$ : number of cycles with stress amplitudes above knee point.
- $n_j$ : number of cycles with stress amplitudes below knee point.

This same equation is applied for normal (to obtain  $\sigma_D$ ) and shear stress (to obtain  $\tau_D$ ). The damage is calculated as follows:

$$D = \frac{\frac{n_{xx}}{N_A} \left( \frac{\sigma_D}{\sigma_R} \right)^2 + \frac{n_{xy}}{N_A} \left( \frac{\tau_D}{\tau_R} \right)^2}{CV} \quad (2.8)$$

where

- $D$ : damage fraction
- $n_{xx}$ : number of cycles in normal loading.
- $n_{xy}$ : number of cycles in shear loading
- $\sigma_R$ : fatigue resistance for normal loading.
- $\tau_R$ : fatigue resistance for shear loading.
- $CV$ : comparison value.

The values for  $D_m$  and  $CV$  change with loading conditions (proportional or non-proportional, constant amplitude or variable amplitude) and are specified in [7] as  $D_m = 0.5$  and  $CV = 0.5$  (non-proportional loading) or  $CV = 1.0$  (proportional loading). The mean stress effect is neglected.

A stress invariant based approach can be found in [52]. This method takes into account load characteristics, load proportionality and mean stress fluctuations in a more sophisticated way. A detailed description of this method is given in Chapter 3.

# 3

## Projection-by-Projection approach

*"Though this be madness, yet there is method in it." – William Shakespeare*

---

### 3.1. General

A method used in this thesis to assess multiaxial fatigue damage is the stress-based Projection-by-Projection (PbP) approach [52]. It is often difficult to correctly account for variable amplitude multiaxial loading with non-zero out-of-phase angles. This methods attempt to account for complex multiaxial stress-states in fatigue damage estimates.

### 3.2. PbP implementation

The PbP approach is a stress invariant based criterion: it considers the amplitude of the second invariant  $\sqrt{J_{2a}}$  expressed by the deviatoric component of the Cauchy stress tensor in a 5-dimensional Euclidean space. To account for non-zero out-of-phase angles in the damage, the load path as described in the 5-dimensional space is projected onto a convenient reference frame by analyzing the covariance matrix associated with the applied stress.

#### 3.2.1. Mathematical properties

The criterion makes use of the amplitude of the second invariant of the deviatoric component of the Cauchy stress tensor and the hydrostatic stress. First, let us define the deviatoric stress tensor as:

$$\boldsymbol{\sigma}' = \boldsymbol{\sigma} - \sigma_H \mathbf{I} \quad (3.1)$$

with  $\sigma_H$  the hydrostatic pressure, defined as:

$$\sigma_H = \frac{1}{3} \text{Tr } \boldsymbol{\sigma} \quad (3.2)$$

and  $\mathbf{I}$  the identity matrix with the same size as  $\boldsymbol{\sigma}$ .

The invariants of any matrix  $\mathbf{A}$  can be calculated using the characteristic equation. A detailed formulation of the characteristic equation and invariants can be found in Appendix A. For now, it is sufficient to know that the invariants can be found by expanding the determinant of  $\mathbf{A} - \lambda \mathbf{I}$ . For a 3x3 matrix, this results in:

$$\det(\mathbf{A} - \lambda \mathbf{I}) = -\lambda^3 + J_1 \lambda^2 - J_2 \lambda + J_3 \quad (3.3)$$

where  $\{J_1, J_2, J_3\}$  are the invariants and all solutions of  $\lambda$  are the eigenvalues. Note here that the hydrostatic stress is defined as the first invariant divided by 3.

The PbP approach uses a 5-dimensional Euclidean space where the length of the vector - let's call this vector  $s(t)$ , see Appendix A - in that space is the second invariant expressed in terms of the deviatoric stress.

This method uses the covariance matrix to find the degree of proportionality of the different terms in the vector  $s(t)$ ; non-proportional loading has covariance 0 and fully proportional loading has covariance 1. The covariance between two random processes is defined as:

$$C_{ij} = \int_T ((x_i(t) - x_{m,i}) \cdot (x_j(t) - x_{m,j})) dt \quad (3.4)$$

with

$$x_{m,i} = \frac{1}{T} \int_T x_i(t) dt \quad (3.5)$$

By projecting the terms in the vector  $s(t)$  along the eigenvectors of the covariance matrix, 5 uniaxial load paths are found with (almost) 0 covariance.

### 3.2.2. Time-domain formulation of the PbP approach

#### *The projection frame of reference*

Accurately addressing the non-zero out-of-phase angles is a complex problem. This method attempts to use the principal axes of the vector  $s$  to account for non-zero out-of-phase angles. The projections of this vector are then treated as non-proportional, uniaxial load paths to assess fatigue damage.

For the sake of clarity, the process of projection is visualized (Figure 3.1) and explained in a 2-D space. Assume two random vibrations  $X_1(t)$  and  $X_2(t)$ . For every  $t$ , the magnitude of the vibrations is plotted as a point  $[X_1(t), X_2(t)]$  in a 2-D space with orthogonal reference frame  $\{X_1, X_2\}$  (black in Figure 3.1). The path that the tip of this vector describes is denoted as the load path  $\Omega$ . Note that the projection of every point  $\Omega(t_i)$  on  $X_j$  is again the magnitude of the vibration of  $X_j(t)$  at time  $t_i$ . Using Equation 3.4, a covariance matrix is set up. The starting hypothesis of this method is that non-zero out-of-phase angles can be accurately taken into account by projecting the load path on the principal reference frame [53]; the reference frame with (almost) zero covariance. This principal reference frame is composed by the eigenvectors of the covariance matrix ( $\{E_1, E_2\}$ , red in Figure 3.1). By projecting the tip of the vector  $[X_1(t), X_2(t)]$  at every time  $t$  on the eigenvectors, we find the magnitude of the vibrations  $X_{p,1}(t)$  and  $X_{p,2}(t)$ , which have, by the definition of the principal reference frame, zero covariance.

#### *Damage evaluation per projected load path*

To assess the damage due to each projected load path, a multiaxial Rainflow counting algorithm was originally introduced in [56]. This technique, while counting cycles on a master channel, simultaneously checks for cycles on an auxiliary channel. Using a modification of the standard Rainflow counting method, fatigue damage is estimated while considering the complex multiaxial load histories. This method uses the deviatoric stress components as the counting channel, while simultaneously recording the maximum hydrostatic stress for each counted cycle. The original Rainflow counting algorithm was first described in [21]. The modified Rainflow algorithm is visualized in Figure 3.3. It shows some projected load path, already reduced to a sequence of tensile peaks and compressive valleys. As the Rainflow algorithm identifies a cycle (Figure 3.3 above) with amplitude  $\sqrt{J_{2a_{ij}}}$  (where  $i$  indicates a projection and  $j$  a cycle), it simultaneously, in the same timespan as the cycle, identifies the maximum value of the hydrostatic pressure  $\sigma_{Hij}$  (indicated by the asterisk in Figure 3.3 below). This process is continued for all cycles. Note that the timespan of multiple cycles may overlap, and that one maximum hydrostatic stress may be found for multiple cycles.

Even though not explicitly elaborated on in the literature read by the author of this thesis, it is worth noting that the choice of the maximum value of the hydrostatic stress, rather than maximum range or mean value of the hydrostatic stress, seems rather odd at first. It is the author's interpretation that the underlying assumption is that negative values of the hydrostatic stress result in less crack growth as they represent a compressive state in the material. It can be observed and easily verified that for certain values of  $\rho_{ref}$ ,  $k_{ref}$  becomes negative which would suggest a longer fatigue lifetime at a higher load amplitude. For this reason, negative values of the hydrostatic stress must be treated with caution.

Multiaxial fatigue damage can now be estimated using a bi-parametric reference SN-curve plotted in a log-log Modified Wöhler diagram (Figure 3.2). The concept of a bi-parametric approach is based on [32, 47]. A reference curve is defined, considering both the mean amplitudes of the counted cycles with respect to the projected load,  $\sqrt{J_{2a_{iref}}}$ , and the mean of all corresponding hydrostatic stress values,  $\sigma_{Href}$ . With the

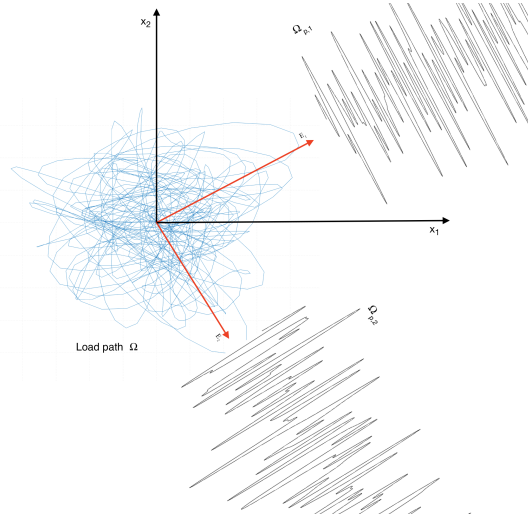


Figure 3.1: Random loading path  $\Omega$  in a 2-D space. The original reference frame is depicted in black, the principal reference frame is depicted in red. The projections are depicted by  $\Omega_{p,1}$  and  $\Omega_{p,2}$  (figure based on [51]).

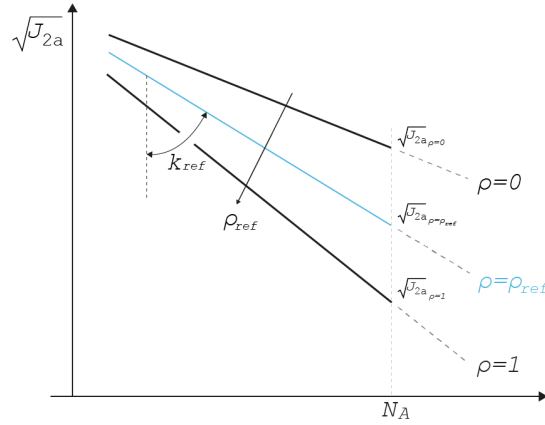


Figure 3.2: Master curves and reference curve plotted in a log-log modified Wöhler diagram (figure based on [52]).

stress-state estimator  $\rho_{ref}$  defined as follows:

$$\rho_{ref} = \sqrt{3} \cdot \frac{\sigma_{Href}}{\left( \sum_i \left( \sqrt{J_{2a_{i,ref}}} \right)^2 \right)^{\frac{1}{2}}} \quad (3.6)$$

with

$$\sigma_{Href} = \overline{\overline{\sigma_{Hij}}} \quad (3.7)$$

and

$$\sqrt{J_{2a_{i,ref}}} = \overline{\overline{\sqrt{J_{2a_{ij}}}}} \quad (3.8)$$

where the double overline indicates a mean over both  $\{i, j\}$  and the single overline indicates a mean over, in this case,  $j$ , a unique reference curve is defined for each time signal. A parameter  $\rho$  was adopted in [47] to take into account mean stress as well as proportionality. The parameter  $\rho_{ref}$  in [52] does not take into account proportionality, as it is assumed to be taken into account when estimated the total damage. The two master curves are defined by a fully-reversed ( $r_l = -1$ ) uniaxial curve, characterized with  $\rho = 1$ , and a fully-reversed torsional curve, characterized with  $\rho = 0$ . This parameter  $\rho$  was adopted to only take into account the effect of the hydrostatic stress.

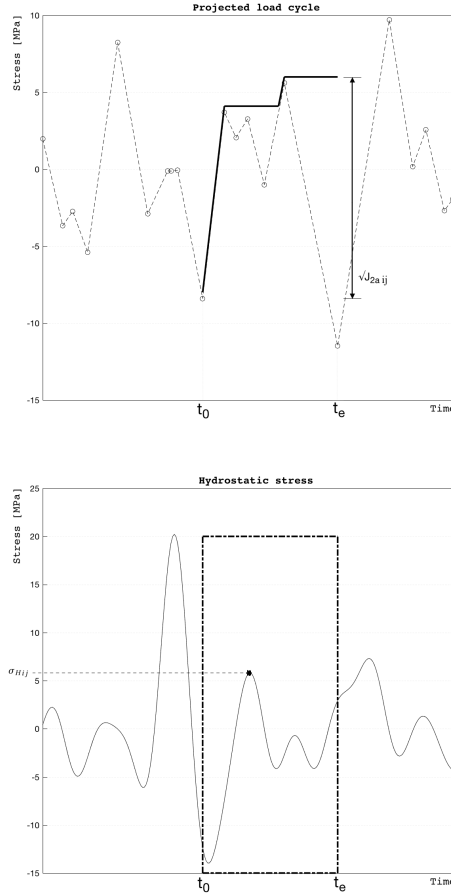


Figure 3.3: As the modified algorithm identifies a cycle (above), it simultaneously checks for the maximum hydrostatic stress (below).

A reference fatigue strength, typically calculated at  $N_A = 2 \cdot 10^6$  cycles, and reference inverse slope of the Wöhler curve are calculated using simple linear relationships [32, 47]:

$$\sqrt{J_{2a_{ref}}} = \sqrt{J_{2a_{\rho=0}}} + \rho_{ref} \cdot \left[ \sqrt{J_{2a_{\rho=1}}} - \sqrt{J_{2a_{\rho=0}}} \right] \quad (3.9)$$

$$k_{ref} = k_{\rho=0} + \rho_{ref} \cdot [k_{\rho=1} - k_{\rho=0}] \quad (3.10)$$

The total damage due to each projection,  $D_i$ , is obtained by applying Miner's rule of linear superposition of damage due to each cycle,  $D_{ij}$ , for every projection [31]. This results in the following expression for the damage related to each projected path  $\Omega_{p,i}$ :

$$D(\Omega_{p,i}) = \sum_j D_{ij} = \sum_j \left( \left[ \frac{\sqrt{J_{2a_{ij}}}}{\sqrt{J_{2a_{ref}}}} \right]^{k_{ref}} \cdot \frac{1}{N_A} \right) \quad (3.11)$$

It is now possible to define an equivalent simplified path,  $\Omega_{eq,i}$  that results in the same damage as the projected path  $\Omega_{p,i}$ . The equivalent simplified path consists of one single cycle with amplitude  $\sqrt{J_{2a_{ieq}}}$  which results in the same damage  $D(\Omega_{p,i})$  so that the equivalent amplitude can be calculated for each projection using the following relationship:

$$\sqrt{J_{2a_{ieq}}} = \sqrt{J_{2a_{ref}}} \cdot (N_A \cdot D(\Omega_{p,i}))^{\frac{1}{k_{ref}}} \quad (3.12)$$

#### Total damage

The total damage due to the considered projections cannot be assumed to be a linear superposition since the damaging events occur at the same time, rather than a sequence of damaging events such as damage due

to cycles. A suitable damage accumulation rule is needed to accurately estimate total damage and take into account the presence of non-zero out-of-phase angles. A quadratic accumulation that was already used in [23], applied to the simplified load paths, is assumed to be most appropriate here:

$$D(\Omega) = D \left( \left( \sum_i \left( \sqrt{J_{2aieq}} \right)^2 \right)^{\frac{1}{2}} \right) \quad (3.13)$$

Note that the quadratic accumulation rule is applied to the equivalent cycles  $\sqrt{J_{2aieq}}$  and not the damage due to these cycles. When substituting the above expression in Equation 3.11, it is interesting to observe that the damage can also be formulated as:

$$D(\Omega) = \left[ \sum_i \left( D(\Omega_{p,i}) \right)^{\frac{2}{k_{ref}}} \right]^{\frac{k_{ref}}{2}} = \left[ \sum_i \left( \sum_j D_{ij} \right)^{\frac{2}{k_{ref}}} \right]^{\frac{k_{ref}}{2}} \quad (3.14)$$

When constant amplitude sinusoidal signals are considered, the PbP approach results in analytical explicit expression for the fatigue damage. Such analytical expressions can be used to provide insight into the influence of certain parameters. Analytical expressions are given in [52]. What's important to remember is that, according to these equations, out-of-phase shear stress do not influence the fatigue damage.

### 3.3. Applicability of the PbP approach

#### 3.3.1. Stress-state estimation

Verification of a model requires extensive model testing, which is not part of this thesis. However, the applicability of the model can be verified for some simple base cases where the outcome is known. A governing parameter in the stress-state estimation is  $\rho_{ref}$ ; its value determines the assumed failure mechanism. The value of  $\rho_{ref}$  is depicted for various loading conditions (biaxial, normal and shear component) in Figure 3.4. The x-axis is labeled such that 0% corresponds to zero normal stress, 100% corresponds to zero shear stress and 50% corresponds to equal amplitudes in normal and shear loading. A reference value based on statistics of the loading is also included, this value is invariant to the type of loading. This reference value is described in [51]. Note that in this figure a biaxial stress-state is assumed. Loading conditions are defined as:

- CA: constant amplitude loading.
- VA - filtered: Variable amplitude loading with frequencies up to  $3rad/s$ .
- VA - unfiltered: Variable amplitude loading with frequencies up to  $60rad/s$ .

It can be concluded that the proposed modified Rainflow algorithm is not applicable with this type of loading, with a maximum absolute percentage error of 115% at unfiltered VA loading. The reference statistical value appears to be capable of accurately estimating the stress-state. Some reference SN-curves are plotted for different values of the stress-state estimator  $\rho_{ref}$  in Figure 3.5. It seems that the applicability of the linearly inter- and extrapolation of SN-curves is limited to  $N_f > 2 \cdot 10^4$  for  $\rho_{ref} = 2$ . To quantify the influence of the stress-state estimator, the estimated number of cycles to failure is calculated for various load conditions (all uniaxial) in Table 3.1. Load case (LC) 1 and 2 have zero-mean hydrostatic stress (load ratio  $r_l = -1$ ), LC 3 and 4 have fully compressive hydrostatic stress ( $r_l > 1$ ). LC 1 and 3 are constant amplitude signals, LC 2 and 4 contain narrow-band noise with a frequency 20 times higher than the signal frequency of LC 1 and 3, with an amplitude that is 50 times lower.

High frequency - low amplitude cycles have an unrealistic influence on the damage estimates, particularly for fully compressive loading. Part of the reason for this can be found in Figure 3.3. Imagine the projected load history is clouded with high frequency - low amplitude cycles. The mean of the maximum hydrostatic stress values  $\sigma_{Hij}$ , in the presence of low amplitude cycles, will converge to the mean of the hydrostatic stress  $\sigma_H(t)$  as the time increment  $t_e - t_0$  (3.3, below) becomes significantly smaller than the zero-up crossing frequency of the hydrostatic stress. Additionally, the denominator in Equation 3.6 will decrease in the presence of low amplitude cycles. The latter influence is stronger, meaning that for zero-mean loading the value for  $\rho_{ref}$  will grow. For compressive loading, a more negative numerator ( $\sigma_{Href}$ ) and a lower denominator result in a  $\rho_{ref}$  value that is far lower in the presence of high frequency - low amplitude cycles. Remember that the slope of the reference SN-curve changes linearly with  $\rho_{ref}$ . Because of the logarithmic nature of fatigue damage,

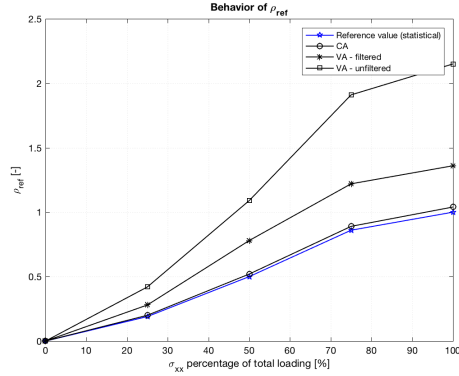


Figure 3.4: The reference parameter  $\rho_{ref}$  for different loading conditions. Filtered means that there are no frequencies higher than  $3rad/s$ , unfiltered contains frequencies up to  $30rad/s$ .

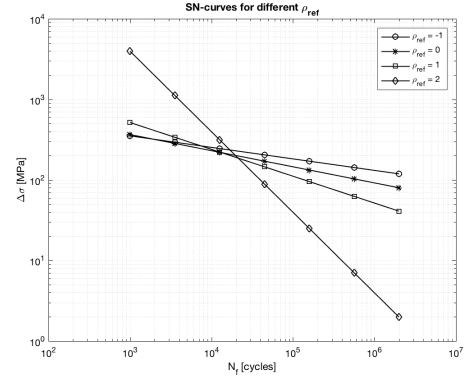
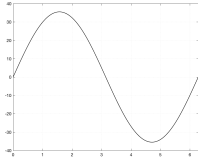
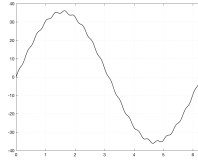
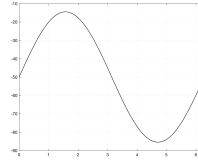
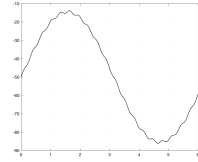


Figure 3.5: Reference SN-curves for different values of the stress-state estimator  $\rho_{ref}$ . Master SN-curve for bending has slope  $m = 3$  and knee-point fatigue strength  $71MPa$ , master SN-curve for torsion has slope  $m = 5$  and knee-point fatigue strength  $80MPa$ . Note that the bending knee-point fatigue strength, expressed in terms of the deviatoric stress tensor, equals  $41MPa$

Table 3.1: Damage estimates by the PbP approach for various load conditions.

Load case 1	Load case 2	Load case 3	Load case 4
$r_l = -1$ - no noise -	$r_l = -1$ - narrow-band noise -	$r_l = 5.6$ - no noise -	$r_l = 5.6$ - narrow-band noise -
			
$\rho_{ref} = 1.00$ $N_f = 2.00 \cdot 10^6$	$\rho_{ref} = 2.91$ $N_f = 5.54 \cdot 10^3$	$\rho_{ref} = -0.41$ $N_f = 2.81 \cdot 10^8$	$\rho_{ref} = -3.85$ $N_f = 5.34 \cdot 10^{15}$

a change in slope has a progressively growing influence on fatigue. Since the slope is higher in compressive loading than in neutral loading, the effect of a slight slope change is higher in compressive loading than in neutral loading.

### 3.3.2. Mean stress effect

The PbP approach adopts the stress-state estimator  $\rho_{ref}$  to estimate the mean stress effect. This reference parameters grows linearly with the hydrostatic stress and can be subdivided into two parts:

- A part that is dependent of the (variable) amplitude of the hydrostatic stress.
- A part that is dependent of the mean hydrostatic stress.

The hydrostatic stress amplitude changes with the loading amplitudes, making the former part approximately constant for loadings of different amplitudes (for example due to different wave heights). However, at a constant mean hydrostatic stress, different SN curves may be found at loadings of different amplitudes; for uniaxial loading with a non-zero mean stress and amplitude that turns to zero,  $\rho_{ref}$  turns to infinity:

$$\lim_{S_a \rightarrow 0} \rho_{ref} = \infty \iff S_m > 0 \quad (3.15)$$

The same goes for multiaxial loading histories. The reference SN-curve is dependent of  $\rho_{ref}$ ; the effect is that damage goes up when the loading amplitude goes down. To quantify, Figure 3.6 depicts two SN-curves: one for uniaxial loading with  $S_m = 0$  (Figure 3.6a), and one for  $S_m = 10$  (Figure 3.6b). Such SN-curves are obtained by calculating the amount of cycles to failure - using analytical expressions - at a discrete set of loading amplitudes. There is not enough evidence available to verify whether this method to take into account the mean stress is applicable for welded joints in frigate type structures.



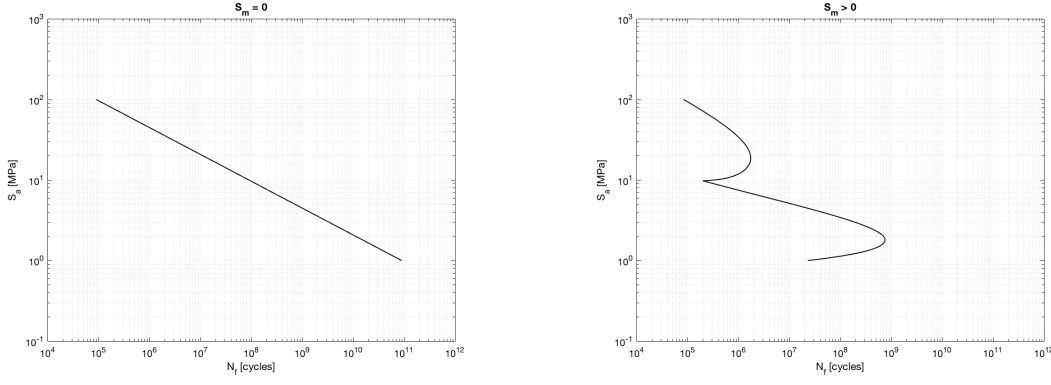
(a) SN-curve for  $S_m = 0$ .(b) SN-curve for  $S_m = 10$ .

Figure 3.6: SN-curves for different values of the mean stress.

### 3.4. A modified approach

#### 3.4.1. General modifications

A modified PbP approach is proposed by the author of this thesis. It was found that the algorithm - using the auxiliary counting channel - does not result in accurate calculations of the stress-state in the investigated cases. Two alternative ways to determine the value of  $\rho_{ref}$  are proposed:

- The modified Rainflow algorithm attempts to identify maxima in the hydrostatic stress for each cycle individually. This is something the statistical value is not capable of. This algorithm is very sensitive to high frequency - low amplitude cycles. A modification is proposed to reduce this sensitivity. A weighted mean to determine  $\sigma_{Href}$  (Equation 3.7) and  $\sqrt{J_{2aifref}}$  (Equation 3.8) is proposed.
- A  $\rho_{ref}$  value based on loading statistics, as described in [51].

To obtain the weighted mean, each individual term in Equations 3.7 and 3.8 was weighted with the magnitude of its cycle:

$$\sigma_{Href} = \frac{\sum_i \sum_j (\sqrt{J_{2aif}} \cdot \sigma_{Hij})}{\sum_i \sum_j \sqrt{J_{2aif}}} \quad (3.16)$$

$$\sqrt{J_{2aifref}} = \frac{\sum_j (\sqrt{J_{2aif}})^2}{\sum_j (\sqrt{J_{2aif}})} \quad (3.17)$$

This yielded better estimates for the stress-state estimator  $\rho_{ref}$  with an absolute percentage error of about 22% at zero-mean unfiltered VA loading. Depending on the master SN-curves and loading conditions, this could still have major consequences for the damage estimates (factor 3 differences in damage for zero-mean uniaxial VA loading have been observed). For this reason, the statistical value for  $\rho_{ref}$  is preferred. It is defined as:

$$\rho_{ref,stat} = \sqrt{3} \cdot \frac{2\sqrt{\text{var}(\sigma_H(t))}}{\left(\sum (\sqrt{J_{2as}})^2\right)^{\frac{1}{2}}} \quad (3.18)$$

where the numerator can be recognized as the significant amplitude of the hydrostatic stress  $\sigma_H(t)$ . The vector  $\sqrt{J_{2as}}$  in the denominator contains the significant wave heights of the components of the deviatoric stress tensor. Note that this  $\rho_{ref}$  value only contains information about the energy in the hydrostatic stress tensor and not the mean offset; the mean stress effect will be discussed in a later stage. Using this  $\rho_{ref}$  value, a threshold value for the knee-point resistance fatigue strength is defined in the same manner as in Equation 3.9. Using this knee-point fatigue strength, a double-slope model can be adopted. The total damage is the sum of the damage in medium cycle fatigue (MCF) and the damage in HCF.

#### 3.4.2. Mean stress effect

The mean stress effect is different in base material than in welds. Welds often have residual stresses that are significantly higher than the mean far-field stress. It is assumed that these residual stresses are implicitly

included in the resistance data. The residual stress in welds typically shows a high amount of scatter [35]. It is therefore important to understand the influence of the residual and mean stress. Moreover, the PbP approach was not solely developed for welded structures. In non-welded structures, the mean stress effect may have a high influence of fatigue damage.

Several methods to account for mean stress are proposed in literature. A couple of methods are discussed in [20] and [33]. Some empirical methods suggest a diagram where the mean stress is plotted on the X-axis and the alternating stress on the Y-axis, with some line defining the safe zone and the unsafe zone. An example is the Goodman relation in [25]. Two points on that line are often defined at a zero-mean stress (the fatigue resistance) and at zero alternating stress (ultimate strength or yield strength). The shape of the line depends on the chosen method. Other methods suggest the use of shifted SN-curves, where a positive mean stress shifts the SN-curve downwards. This method requires extensive testing to accurately describe the effect of various parameters such as the load ratio, hydrostatic stress or maximum normal stress on a critical plane. Lastly, some methods suggest the superposition of the mean stress (or hydrostatic stress) on either a component of the Cauchy stress tensor (Dang Van [12]) or on an invariant of the Cauchy stress tensor (Sines [22]) to obtain fatigue damage. Two methods to include the mean stress were investigated. Both methods will be discussed here shortly.

#### *Mean stress correction on a critical plane*

This method is based on Dang Van [12]. A main assumption in this method is that a crack will grow on the plane that experiences the highest normal stress. Highest in this context means the plane that, in time, experiences the most energy in a particular normal loading direction. Preferably, every counted cycle in this loading direction will be individually corrected using the hydrostatic stress. This is unfortunately not possible since the rainflow counting algorithm is used after the loading has been projected on the eigenvectors of the covariance matrix. Instead, the stress time history is multiplied by a factor such that the significant amplitude is corrected using the hydrostatic stress. Since no other evidence is available to the author of this thesis, a Goodman diagram [25] was used to calibrate this factor.

This factor is a function that depends on the ultimate strength and mean hydrostatic stress. Using the Goodman diagram, it is relatively easy to find an equivalent amplitude for CA loading. It appears that the best function fit, relating the equivalent amplitude to the loading amplitude, is:

$$S_{eq} = \exp(\ln(S) \alpha \cdot \sigma_{Hmean}) \quad (3.19)$$

with

$$\alpha = \beta \left( 1 + \frac{\ln(\sigma_{UTS}) \cdot q}{(1 - |q|) \sigma_{UTS}} \right) \quad (3.20)$$

and

$$q = \frac{\sigma_{Hmean}}{\sigma_{UTS}} \quad (3.21)$$

where  $\beta$  represents some dimensionless material factor. Note that this function also fits the boundary condition; the amplitude goes to infinity when the absolute mean hydrostatic stress equals the ultimate strength.

The advantage of this method is that it utilizes the hydrostatic stress, same as the original PbP approach. An obvious disadvantage is that it has no mathematical or physical basis.

#### *A walker correction*

The Walker model [57] uses the load ratio of a particular cycle to correct for its mean. It is important to realize that the cycle amplitude and load ratio fully define all properties of a cycle. The equivalent amplitude is defined as:

$$S_{eq} = \frac{S}{(1 - r)^{1-\gamma}} \quad (3.22)$$

In this equation,  $\gamma$  defines the relative influence of the amplitude and the mean of a cycle. It has to be taken into account that negative shear stresses have no physical meaning. The nature of the loading makes it very awkward to accommodate for this fact, especially since its projected load paths that are being used in the Rainflow counting algorithm rather than actual load paths. There is no obvious way to manipulate the load ratio such that it will not distinguish negative values, while simultaneously giving more weight to cycles with a higher mean. Furthermore, there is no obvious mechanism - like crack opening and closing for normal loading - that suggests mean shear stresses influence fatigue. To account for this, it is proposed to set the mean shear stress to 0, and multiply the stress time history by 2. In this way, the base case for pure tension

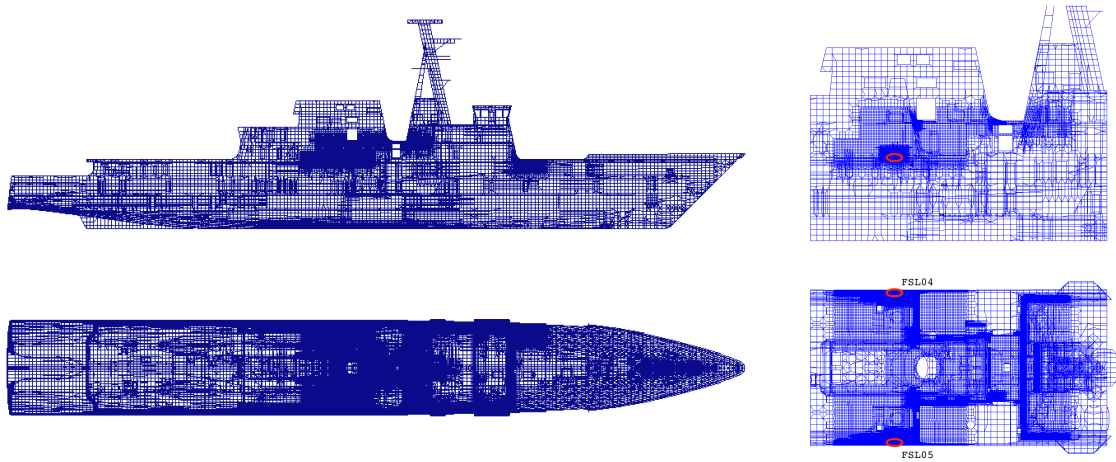


Figure 3.7: Location of FSL04 and FSL05.

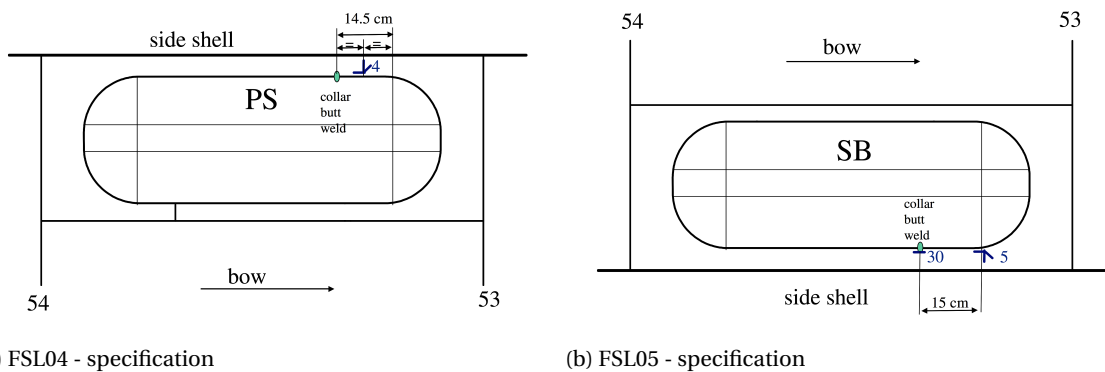


Figure 3.8: Top view detail of FSL04 and FSL05.

will result in the correct amount of cycles to failure.

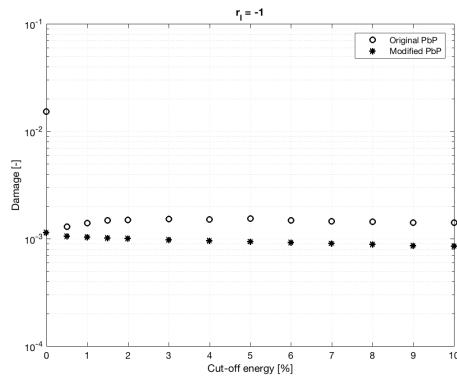
The latter method is preferred over the former since it has a sounder foundation. There is evidence available in [43] that fatigue failure can be related to the load ratio and amplitude of a cycle. The *Mean stress correction on a critical plane* is constructed out of function fits and other parameters that have no mathematical basis. It will have to be investigated if the Walker correction approach is valid when applied to projected load paths of the deviatoric stress.

## 3.5. Validation

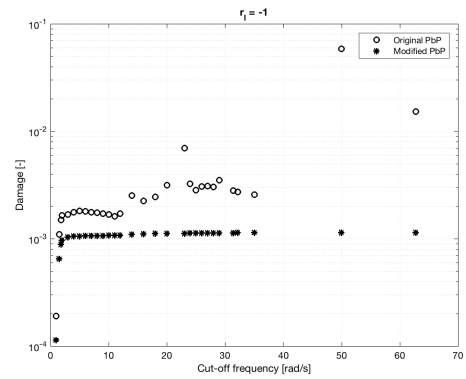
### 3.5.1. Method of validation

A sensitivity study showed that high frequency - low amplitude cycles have high influence on the damage estimates obtained by the PbP approach. The effect of these cycles will be made clear by gradually filtering the stress time histories. Strain gauge data is used to investigate the effect of these cycles. To exclude local effects introduced by welds, data measured at cold spots will be used for this part of the validation. Multi-axial data is available for Fatigue Sensitive Location (FSL) number 04 and 05; their location in the vessel and a detailed view are depicted in Figure 3.7 and Figure 3.8 respectively. Due to FSL05 being closer to a bend, more shear stress is present than in FSL04. This location is selected for this part of the validation.

An energy filter and a low-pass frequency filter are introduced. A particular stress time history is transformed to frequency domain using a Fast Fourier Transform (FFT, [36]). The low-pass frequency filter sets all frequencies higher than a certain cut-off frequency to zero. The energy filter calculates the cumulative power spectral density. Frequencies that contribute to the upper  $x$  percent of the total power, are set to zero. Here  $x$  is the cut-off energy. The spectrum is transformed back to time domain using an inverse FFT. Since the PbP

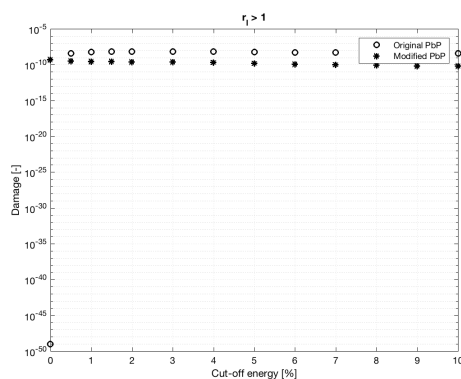


(a) Energy filter.

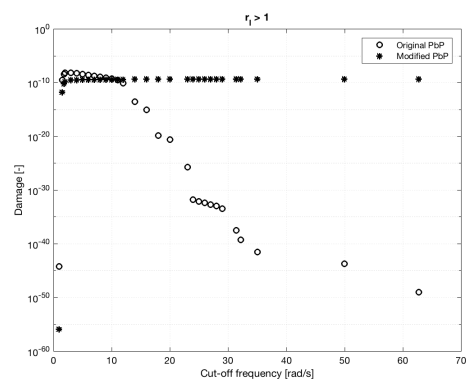


(b) Frequency filter.

Figure 3.9: Damage estimates for filtered stress time histories at zero-mean hydrostatic stress. An energy filter (3.9a) and a frequency filter are used (3.9b).



(a) Energy filter.



(b) Frequency filter.

Figure 3.10: Damage estimates for filtered stress time histories at fully compressive hydrostatic stress. An energy filter (3.10a) and a frequency filter are used (3.10b).

approach takes into account the hydrostatic stress level, a distinction is made between zero-mean loading ( $r_l = -1$ ) and fully compressive loading ( $r_l > 1$ ). It is assumed that 3hour data is sufficient to obtain accurate results. The results are depicted in Figures 3.9 and 3.10. These figures include the original PbP approach and the modified PbP approach. Note that, in order to make a valuable comparison, the mean stress effect must be taken into account similarly in both approaches: both with a linearly interpolated SN-curve.

### 3.5.2. Results and discussion

A couple of things can be observed:

- The damage estimates show large fluctuations in Figure 3.9b as a result of the modified Rainflow algorithm.
- The 3% energy at the high frequency end of the power spectral density function (the data between a cut-off energy of 0% and 3% in Figure 3.9a) results in a damage magnification of a factor 10. From Figure 3.9b can be observed that this energy is stored in frequencies from  $5\text{rad/s}$  tot  $65\text{rad/s}$ .
- A similar type of observation is made in Figures 3.9b and 3.10b, only now the energy stored in frequencies from  $2\text{rad/s}$  to  $65\text{rad/s}$  reduce the damage by a factor  $10^{-40}$ .
- The maximum wave excitation is expected around  $0.5$  to  $1.5\text{rad/s}$ . The bending frequencies start around  $12\text{rad/s}$  (2-node bending); higher bending modes have higher frequencies. The results for the original PbP approach suggest that these eigenmodes either magnify the damage estimates drastically when the mean stress is positive (up to a factor 10 in the investigated case), or reduce the damage drastically when the mean stress is negative (up to a factor  $10^{-40}$  in the investigated case).

---

An explanation for this was already given in Section 3.3.1. It can be concluded that, in the investigated cases, the spectral stress-state estimator  $\rho_{ref}$  (Equation 3.18) behaves better than the proposed modified Rainflow algorithm.



# 4

## Research methodology

*"If I had an hour to solve a problem I'd spend 55 minutes thinking about the problem and 5 minutes thinking about solutions." – Albert Einstein*

---

### 4.1. General

A quantitative study was performed on the influence of multiaxial stress states on fatigue damage in the USCG Cutter Bertholf. This chapter describes the specific methods for the collection of data, how it was processed and how the data was analyzed.

### 4.2. Instrumentation and gathered environmental data

The study focused on 5 days in the month July of the year 2011. During this period of time, the USCG Cutter Bertholf sailed back to port at an approximate speed of 15knots. It was shown that a significant amount of fatigue damage (obtained using a uniaxial fatigue damage model) could be contributed to this period ([26]).

Strain measurements were performed using local unidirectional strain gauges and rosettes. A total of 19 fatigue sensitive locations were instrumented. Unidirectional fatigue damage calculations in [26] showed that FSL01, FSL02 and FSL03 experienced the highest fatigue damage. FSL04 and FSL05 were instrumented with rosettes. The locations and a description are depicted in Table 4.1 and visualized in Figure 4.1. The USCG Cutter was also instrumented with Rosettes. This data will be processed using the model that was developed to estimate multiaxial fatigue damage.

To monitor wave conditions, the USCG Cutter Bertholf was equipped with the WaMoS Wave Radar [5, 27]. The WaMoS Wave Radar provides 2D-frequency direction wave spectral densities. A data fusion approach as described in [50] was used to improve the energy content of the spectral densities. The RMS of the measured pitch motion of the Cutter is compared to a calculated RMS pitch motion. The ratio of the measured and calculated RMS values is used to update the spectral densities. The accuracy of this method fully depends on the accuracy of the computed pitch transfer function (TF) and measured pitch motion. The imaging mechanism requires a minimum wind speed of  $3m.s^{-1}$ ; significant wave heights below  $0.5m$  cannot be resolved by the system and heavy persistent rain showers will not allow for wave measurements. Some properties and the corresponding ranges and accuracy are summarized in Table 4.2.

### 4.3. Methods of research

#### 4.3.1. Model calculations

The research utilized potential theory to model the flow of water around the vessel. A user defined set of Airy waves with unique combinations of frequency and wave directions was used to calculate pressures on the hull; the underlying assumption is that a random wave can be described by this set of Airy Waves. Integrating

Table 4.1: Data on strain measurements.

FSL #	Location	Description
01	02 Deck	Weld frame 52, starboard side (Further specified later).
02	02 Deck	Weld frame 52, port side (Further specified later).
03	02 Deck	Location defined by horizontal bracket (see Figure 4.2).
04	01 Deck	Between frame 53 and 54, port side. On edge of an air intake vent (see Figure 3.8a).
05	01 Deck	Between frame 53 and 54, starboard side. On edge of an air intake vent (see Figure 3.8b).

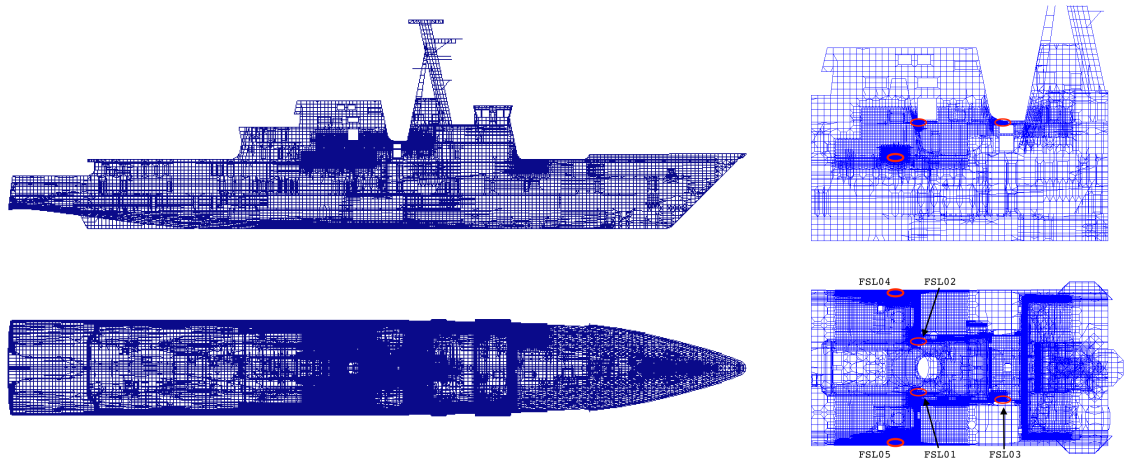


Figure 4.1: Location of FSL{01,02,03,04,05}.

the pressures results in harmonic nodal forces. A finite element (FE) solver was used to calculate transfer functions for every unique combination of frequency and wave direction. The transfer functions were interpolated between wave directions and vessel speeds using a cubic spline to obtain a finer grid. A boundary condition was imposed such that the value and derivative of the transfer function at  $0^\circ$  was, by approximation, equal to value and derivative at  $360^\circ$ . Multiplying the transfer function squared with the wave spectrum (taking into account the heading) results in a 3-D response spectrum; integrating this response spectrum over the wave directions yields the 2-D response spectrum. Note that this 2-D response spectrum holds no information about the random wave phase. Wave spectra were averaged every half hour, thus a response spectrum exists for every half hour, for every stress component.

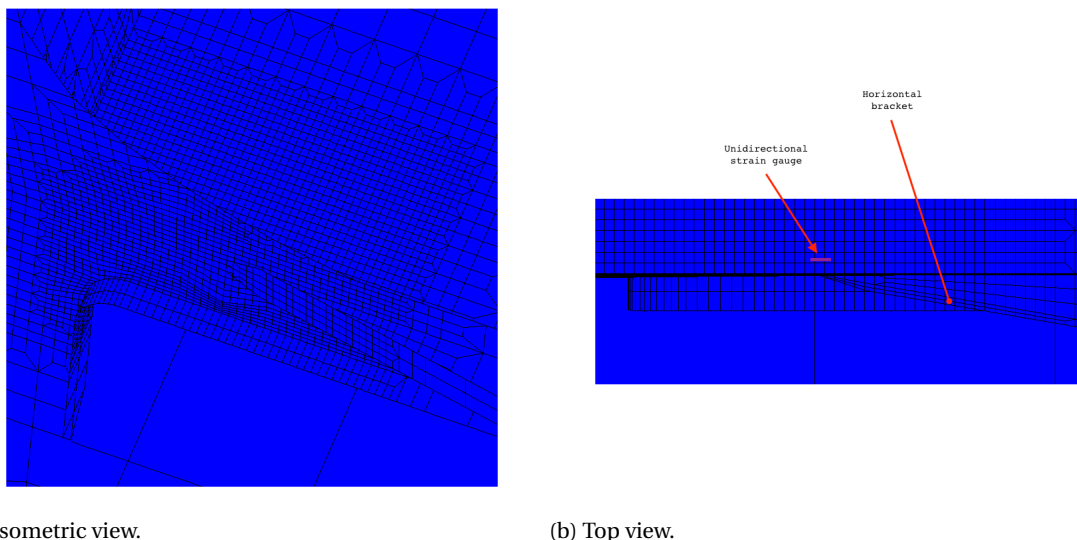
Since the wave phase is unknown, a number of realizations were made per stress component (per half hour). The number of realizations depends on the convergence of the damage estimate. To take into account the covariance between stress components, the different stress components had to be discretized at the same frequencies. The discretization was performed using the concept of 'equal-energy-bins' (Figure 4.3). A reference spectrum was obtained by a weighted sum of the spectra per stress component. The weights were chosen such that the energy per spectrum (area under the spectrum) was equal. The total area of the reference spectrum was subdivided in bins of equal energy. The centroids of the bins are the discretization frequencies. A linearly spaced array of frequencies was added to make sure that every part of the spectrum is well represented. The amplitude is then:

$$A = \sqrt{2 \cdot E} \quad (4.1)$$

### 4.3.2. Data post processing

Calculations were performed in frequency domain and time domain. The strain measurements were transformed to frequency domain using a FFT. Each stress time history was subdivided into segments. The segments were chosen such that the resolution is better than the resolution of the wave spectra, with 50% overlap.





(a) Isometric view.

(b) Top view.

Figure 4.2: Specification of FSL03.

Table 4.2: Specifications wave radar system.

Property	Range	Accuracy
2-D frequency direction spectrum	0.02 - 0.35 Hz 0 - 360°	-
Significant wave height	0.5 - 20 m	+/- 10% or +/- 5 m
Mean and peak period	3.5 - 40 s	+/- 0.5 s
Mean wave directions	0 - 360°	+/- 5°

## 4.4. Data analysis

### 4.4.1. General

The main objective is to investigate the effect of multiaxial stress-states on fatigue damage in frigate type structures. All damage calculations will be done using the modified PbP approach and IIW design rules.

### 4.4.2. Environmental data

Wave data is available from July 6 to July 11 in 2011 (From the WaMoS Wave Radar). A 3-D spectrum is available every half hour. A wave can be described by the following characteristics:

- Significant wave height  $H_s$ .
- Peak period  $T_p$ .
- Incoming wave direction  $\theta_I$ .
- Wave spreading  $\theta_{spr}$ .

The wave data was analyzed using Xwaves [41]. The software identifies different wave components in a 3-D wave spectrum. In the 5 days of data that was investigated, spectra that contain more than one component were found about 60% of the time. Spectra containing more than two components were not found in the data. This poses two problems:

- Spectra where only one component was found do not consider all the energy in the spectrum. Frequencies and wave directions that contain energy, but are not assumed to be part of the wave component nor a wave component by itself, are neglected. The result is that approximately 25% of the energy is not taken into account in the wave characteristics.
- When two wave components are present, eight wave characteristics are necessary to define the full spectrum. All these eight parameters include a section of the 3-D wave spectral energy.

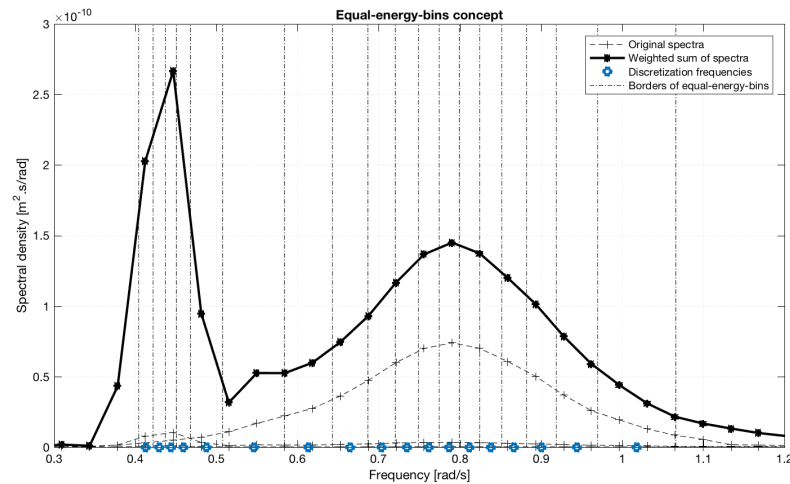


Figure 4.3: Conceptual explanation of the equal-energy-bins concept. The area between the borders is, by numerical approximation, equal. Note that the linearly spaced array of frequencies is not included in the figure.

The relative influence of the separate wave components has to be taken into account explicitly. To do so, dependent parameters can be defined that fully define a 3-D wave spectrum and the relative influence of the separate wave components. It was attempted to fully define a 3-D wave spectrum using 3 parameters: significant wave height, the incoming peak wave direction and a spreading parameter. The peak period and wave height show a strong correlation [34], it is assumed that the peak period is implicitly included in the wave height. A new spreading parameter is introduced that attempts to define the distribution of energy throughout the spectrum. Doing so, it takes into account the relative influence of the separate wave components implicitly. The wave spreading parameter is defined as:

$$\theta_{spr} = 2 \cdot \frac{\int_{\theta_I-180}^{\theta_I} (\theta_I - \theta) \cdot E_\theta(\theta) d\theta + \int_{\theta_I}^{\theta_I+180} (\theta - \theta_I) \cdot E_\theta(\theta) d\theta}{360 \cdot \max E_\theta(\theta)} \quad (4.2)$$

A detailed elaboration on this wave spreading parameter, the incoming peak wave direction and  $E_\theta$  (Spectral wave energy density as a function of wave direction) is included in Appendix B. This appendix will elaborate on the behavior of the spreading parameter, both for confused sea-states as well as sea-states that only contain one wave component.

To reinforce the calculations a number of 3-D wave spectra were modeled, based on the Global Wave Statistics for the North Pacific [34]. The Global Wave Statistics provide the probability of occurrence of a sea-state with a particular wave height and period. A single sea-state consists of a swell and a wind wave; no correlation between the two was taken into account. A two-parameter Pierson-Moskowitz spectrum was assumed to model the waves since it allows for the input of both significant wave height and peak frequency. Swell and wind waves are modeled with a wave direction (relative to true north) of  $0^\circ$  to  $315^\circ$  each, with an increment of  $45^\circ$ . All possible combinations between swell and wind waves are made. The global wave statistics do not specify the directional spreading. A directional spreading function must allow for the input of a spreading parameter while the area under the function remains equal to 1, such as a cosine-power [15] or circular normal spreading function [9]. A normal distribution was fitted to the directional spreading of spectra that contained only one wave component. The mean value of the standard deviation was chosen as the spreading for the swell component. The wind component is assumed to distribute the energy over twice as many wave direction (i.e.: the spreading, modeled by a standard deviation, was twice as high). The modeled wave heights and corresponding peak periods are summarized in Table 4.3. The spreading as a function of the wave height is depicted in Figure 4.4 (remember that the spreading parameter in Equation 4.2 takes all present wave components into account) and the mean frequency as a function of the wave height is depicted in Figure 4.5. Since the vessel heading is random, the wave direction relative to true North is of no influence on the incoming wave direction (relative to the vessel).

The simulated waves seem to underestimate the spreading at lower waves. Lower waves correspond to higher frequencies. Measured waves contain white noise; this noise becomes more relevant for higher frequencies due to the lower peak frequency. White noise is not modeled in the simulated waves, effectively

Table 4.3: Summary of modeled waves.

Wave type	{Wave heights modeled [m], Corresponding peak periods [s]}
Swell waves	{0.89, 3.2}; {1.24, 6.3}; {3.77, 10.9}; {6.96, 16.4}
Wind waves	{0, n/a}; {0.89, 3.2}; {1.24, 6.3}; {3.77, 10.9};

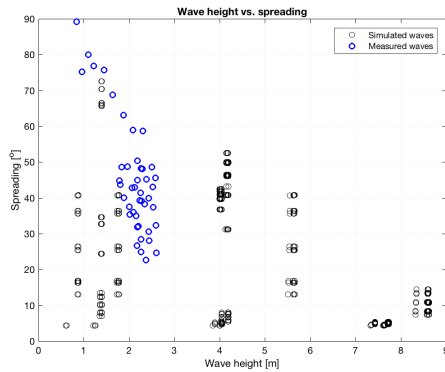


Figure 4.4: Spreading as a function of wave height.

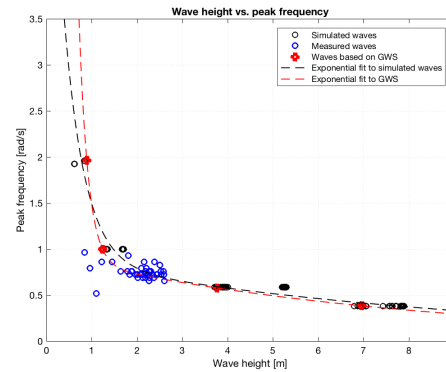


Figure 4.5: Mean frequency as a function of wave height.

reducing the spreading. The spreading appears to be smaller between wave heights of 7m and 8m than at surrounding wave heights. This is because this particular wave spectrum only consists of a swell wave. Waves between 8m and 9m also contain a wind component. The measured wave data seems to agree with the Global Wave Statistics. Since the modeled waves are comprised of a swell and a wind component, of which each separate component is modeled according to the Global Wave Statistics, the combined sea-state differs slightly from the Global Wave Statistics.

#### 4.4.3. Investigation of the effect of multiaxial stress-states on fatigue damage in frigate type structures

##### Strain gauge based data

Measured data to investigate the effect of multiaxial stress-states on fatigue damage is available for FSL04, FSL05 and from another frigate: the USCG Cutter Stratton. No manipulations were performed on this data. Measured data is valuable because quality of the outcome solely depends on the quality of the strain gauges and the method used to estimate fatigue damage. The Stratton data lacks detailed information on the sea-state, but covers a period of two years; the validity of the conclusions is extremely dependent of the (unknown) encountered sea-states. The Bertholf data includes the 3-D wave spectra, but only covers a period of 5 days.

##### Transfer function based data

This part of the study focused on FSL01 and a reference location. TFs were available for a vessel speed of 16knots, at 7 wave directions:  $0^\circ$  to  $315^\circ$  with an increment of  $45^\circ$ . A specification of FSL01 is depicted in Figure 4.6. An FE model of the detail was constructed. It was assumed that the total loading is the sum of three load conditions:

- Pure tension in local  $x$ -direction,  $F_{xx}(t)$ .
- Pure tension in local  $y$ -direction,  $F_{yy}(t)$ .
- Pure shear,  $F_{xy}(t)$ .

If the stresses in time at any location in the FE model are known, the magnitudes of the three load conditions (in time) can be calculated using a conversion matrix. This conversion matrix is unique for every location in the FE model. Similarly, the stresses in time at any location in the FE model can be calculated as a linear superposition of the three load conditions. The FE model contains sharp notches, singularities in the FE model lead to inaccurate estimations of the stresses at these notches. A method as described in [19] was used to estimate this hot spot stress. This method and the FE model are further elaborated on in Appendix C.



(a) Isometric view.

(b) Detailed view.

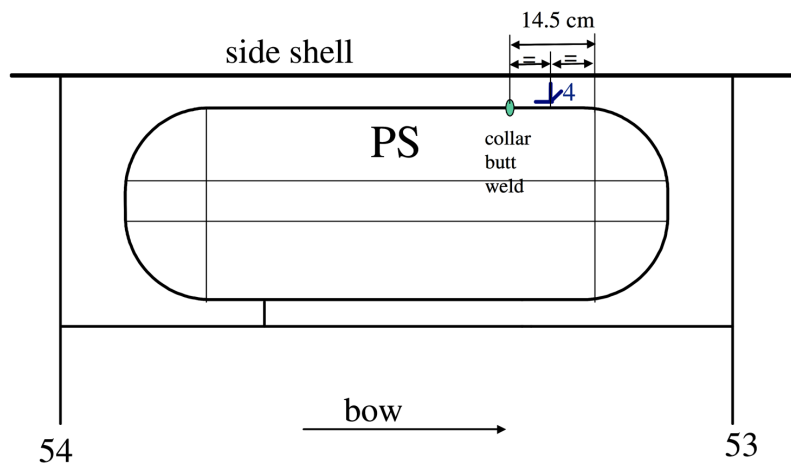
Figure 4.6: Specification of FSL01.

Table 4.4: Summary of the investigated data.

Data type	Specification	Stress concept	Comments
Transfer function based	Reference location	Cold spot	Reference value
	Reference location	Hot spot	In combination with detail FSL01
	FSL01	Hot spot	-
Strain gauge based	FSL04	Cold spot	-
	FSL05	Cold spot	Near a bend
	Stratton Data	Hot spot	Near a weld.

Theoretically, this detail could be present at every location in the vessel. This means that any cold spot stress time history, in combination with a convenient (yet realistic) conversion matrix, theoretically results in realistic hot spot stress time histories. Transfer functions of FSL01 are available. The location (in the FE model) that the TFs correspond to is known, so the conversion matrix is known too. TFs are also available for a location near FSL04, referred to as the reference location (specified in Figure 4.7). Since the longitudinal loading is dominant, the location in the FE model that was used to set up the conversion matrix was chosen at the same global  $y$ -coordinate, at a distance from the FSL such that the derivative of the stress in global  $x$ -direction to  $x$  is approximately 0 (i.e.: the notch no longer affects the stress distribution in  $x$ -direction). These TFs are also used without the hot spot correction to obtain a reference value.

All investigated data (including strain gauge based data) is summarized in Table 4.4.



Reference location



Figure 4.7: Specification of the reference location.



# 5

## Results and discussion

*"We are all born ignorant, but one must work hard to remain stupid" – Benjamin Franklin*

---

### 5.1. General

In this chapter, all results will be presented and discussed. This chapter will consist of three sections. Firstly, some expected results are presented. The second section will present the results; the relation between uniaxial damage and multiaxial damage is presented and discussed, and the correlation with certain wave statistics is investigated. Lastly, all presented results will be discussed. Note that, unless specified otherwise, damage is expressed in number of cycles to failure  $N_f$ .

### 5.2. Expected results

#### 5.2.1. Maximum response

Torsion is a result of forces that are not applied on the shear center of a ship's cross-section. The maximum torque is present when the moment applied at the bow of the vessel is opposite in sign from the moment applied at the stern of the vessel. The maximum moment, in any location in the vessel is applied when the encountered waves have an incoming direction of  $45^\circ$  wave respect to the heading. The moments are opposite in sign when the length of the vessel projected on a line parallel to the wave direction equals half of the wave length. This principle is illustrated in Figure 5.1.

The length of the vessel projected on a line parallel to the wave direction, in bow or quartering waves, equals:

$$l_p = \frac{l}{\sqrt{2}} \quad (5.1)$$

This means that the wave length that results in the maximum torque is:

$$\lambda = 2 \frac{l}{\sqrt{2}} \quad (5.2)$$

The dispersion relation for deep water is [6]:

$$\lambda = \frac{g}{2\pi} T^2 \quad (5.3)$$

Using the dispersion relation, it is expected that the maximum torque is present in waves with a wave length of  $\lambda = 170m$  (assuming an effective length of  $120m$ ), with a corresponding period of  $10.4s$  or frequency of  $0.60rad/s$ . The sagging and hogging response has a maximum when the wave length equals the length of the vessel. Again, assuming an effective length of  $120m$ , this results in a maximum sagging and hogging response at a frequency of  $0.72rad/s$ .

The software used to calculate the transfer functions takes vessel speed into account by calculating encounter frequencies. It is worth mentioning the velocity is also included in Potential Theory, the theory used

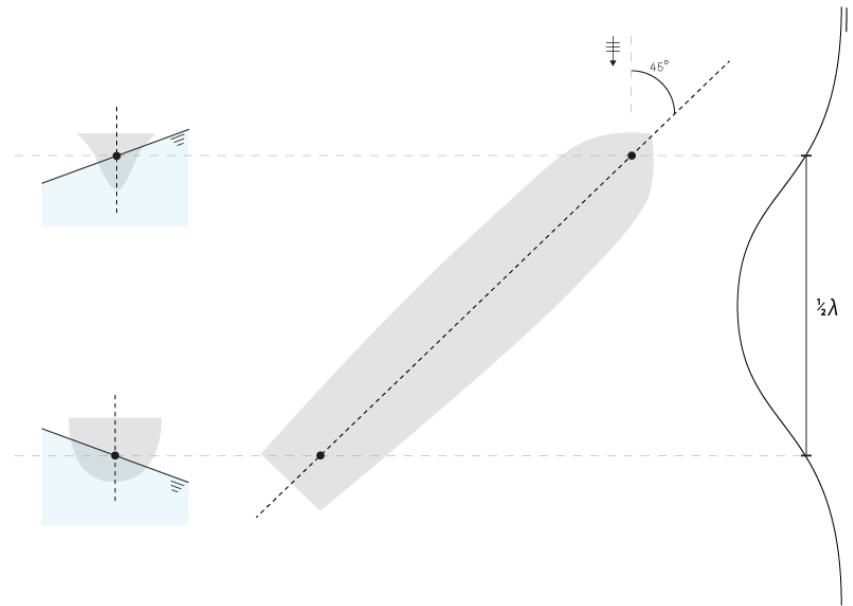


Figure 5.1: Maximum torsion in ships.

by the software to model the flow around the vessel. The maximum forced torsion response and maximum sagging and hogging response are a function of wavelength, which doesn't change with vessel speed. It is not known how, and if, the software deals with this. According to the theory of encounter frequencies, the maximum torsion response is expected at a frequency of  $0.63\text{rad/s}$  (bow waves) and  $0.57\text{rad/s}$  (quartering waves), and the maximum hogging and sagging response is expected at a frequency of  $0.78\text{rad/s}$  (head waves) and  $0.65\text{rad/s}$  (following waves). The transfer functions are depicted in 5.2.

The analytical calculations do not fully agree with the transfer functions. It is observed that the maximum torsion response is obtained in bow waves, at a frequency of  $0.47\text{rad/s}$ . The maximum sagging and hogging response is obtained in head and following waves at a frequency of  $0.79\text{rad/s}$ .

### 5.2.2. Proportionality

The level of proportionality influences the fatigue damage. Multiaxial stress-states occur due to geometry changes (proportional in nature) or due to multiaxial loading (often non-proportional). To demonstrate this principle, correlation coefficients are computed for a reference cold spot and a reference hot spot (HS) location as a function of the incoming wave direction. This correlation coefficient equals 1 IP stress-states, 0 for OP stress-states and -1 when the stress-state is in anti-phase (AP). Loading in longitudinal direction is governing in frigate type structures. Correlation coefficients are calculated between longitudinal and transverse stresses, and longitudinal and shear stresses. The results are depicted in Figure 5.3 for the reference cold spot and Figure 5.4 for the reference HS.

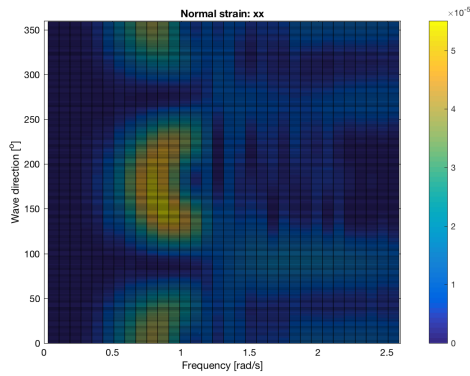
When the HS location is considered, the stress-state is almost completely IP for every sea-state. This suggests that the geometry induced transverse and shear loading are far bigger than the multiaxial loading induced transverse and shear loading. A clear correlation can be observed between incoming wave direction and stress-state proportionality, and wave height and stress-state proportionality. Proportionality depends on incoming wave direction because of the structural response. The structural response, as discussed in Section 5.2.1, is different for different peak frequencies and thus wave heights.

## 5.3. Results

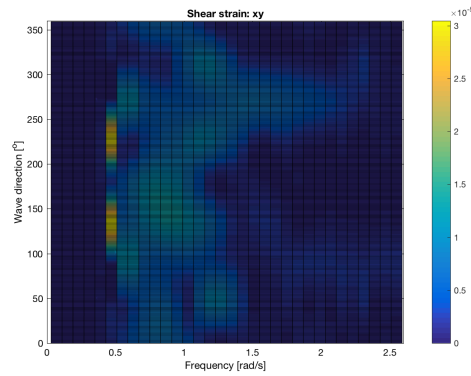
Firstly, the relation between uniaxial damage and multiaxial damage is investigated. Secondly, the correlation between damage and wave characteristics is investigated.

### 5.3.1. Uniaxial vs. multiaxial damage



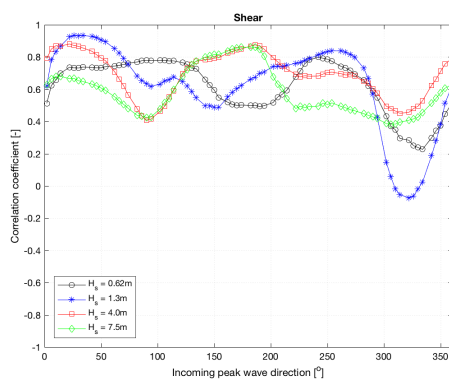


(a) Transfer functions for  $\epsilon_{xx}$ .

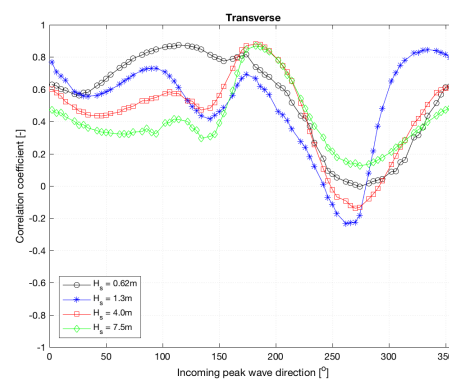


(b) Transfer functions for  $\epsilon_{xy}$ .

Figure 5.2: Transfer functions at a vessel speed of 15 knots.

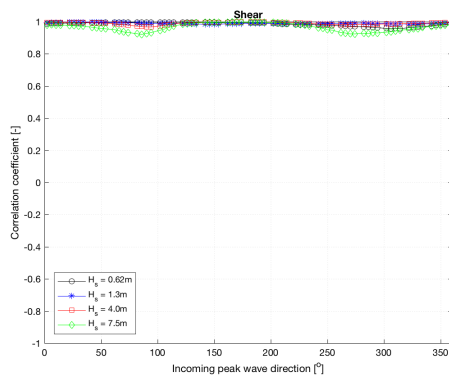


(a) Correlation with shear stress.

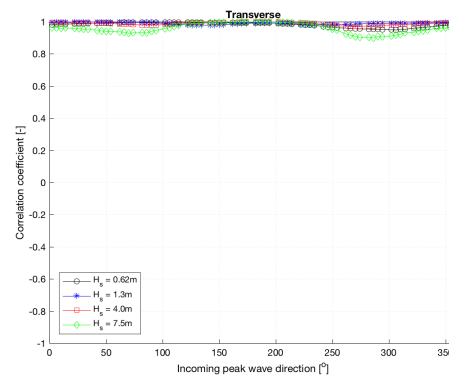


(b) Correlation with transverse stress.

Figure 5.3: Level of proportionality for the reference cold spot.



(a) Correlation with shear stress.



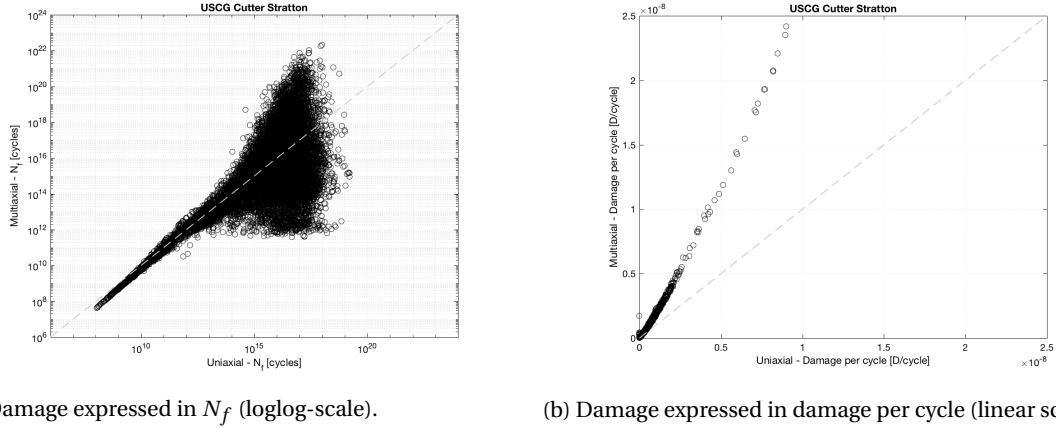
(b) Correlation with transverse stress.

Figure 5.4: Level of proportionality for the reference HS.

**Results**

The multiaxial damage (expressed in  $N_f$ ) is plotted against the uniaxial damage. Data based on transfer functions was calculated using simulated waves (see Table 4.3) and waves measured aboard the USCG Cutter Bertholf. Strain gauge (SG) data was available for FSL04 and FSL05.

As a reference, Figure 5.6 shows the results using analytical expressions. Remember that all damage calculations were performed using the IIW design rules and (modified) PbP approach. The IIW design rules do not take into account loading in transverse direction; the PbP approach does not account for phase shifts in

(a) Damage expressed in  $N_f$  (loglog-scale).

(b) Damage expressed in damage per cycle (linear scale).

Figure 5.5: Damage estimates from the USCG Cutter Stratton.

shear loading (Chapter 3). OP is defined by a phase angle of  $90^\circ$ , AP is defined by a phase angle of  $180^\circ$ . Four cases (for the analytical expressions) were considered:

- $\tau_{xy} = 0$ , IP: biaxial normal loading, in-phase.
- $\tau_{xy} = 0$ , AP: biaxial normal loading, anti-phase.
- $\sigma_{yy} = 0$ , IP: biaxial loading comprised of normal and shear, in-phase.
- $\sigma_{yy} = 0$ , OP: biaxial loading comprised of normal and shear, out-of-phase.

Longitudinal stress  $\sigma_{xx}$  is assumed to be always present. The black and blue line in Figure 5.6 correspond to IP (correlation coefficient of 1) and AP (correlation coefficient of -1) loading. If non-proportional loading is considered (correlation coefficient of 0), the result lies between the black and blue line.

Figures 5.7, 5.8, 5.9 and 5.10 respectively depict the results for FSL01 (TF based), FSL04 and FSL05 (SG based), the reference location using a cold spot approach and the reference location using a HS approach in combination with the structural detail from FSL01 (both TF based). Every point in the figures represent 3hours of data for the measured waves and 30minutes of data for the simulated waves. Each figure contains four pieces of information:

- Simulated waves, damage calculated using the PbP approach (in black).
- Simulated waves, damage calculated using the IIW design rules (in red).
- Measured waves, damage calculated using the PbP approach (in blue).
- Measured waves, damage calculated using the IIW design rules (in green).

Figure 5.5 depicts the damage estimates obtained at the USCG Cutter Stratton. The damage is expressed in number of cycles to failure (Figure 5.5a) and damage per cycle (Figure 5.5b).

### Considerations

The slope change in the lines in Figure 5.6 are due to the double slope model. This is present in both the IIW design rules and PbP approach. Part of the AP loading (no shear, blue line) as calculated by the PbP approach lies above the  $x = y$  line, which means that the lifetime is longer when only normal stress in  $x$ -direction is considered. Let's consider an original plane with two normal stress:  $\sigma_{xx}(t)$  and  $\sigma_{yy}(t)$ , where  $\sigma_{xx}(t) = -\sigma_{yy}(t)$  (AP biaxial normal loading). There is no shear stress acting on this plane. According to Mohr's circle, a plane that is rotated  $45^\circ$  with respect to the original plane will have only shear stress  $\tau_{xy}(t)$ , with amplitude equal to the amplitudes of  $\sigma_{xx}(t)$  and  $\sigma_{yy}(t)$  from the original plane, and no normal stresses. It makes sense that the damage calculated using the original plane should be equal to the damage calculated using the rotated plane. A uniaxial approach assumes  $\sigma_{yy}(t) = 0$ ; fatigue damage would be calculated using only  $\sigma_{xx}(t)$  with a normal stress SN-curve. The multiaxial approach effectively uses  $\tau_{xy}(t) = \sigma_{xx}(t) = -\sigma_{yy}(t)$  (the rotated plane) with

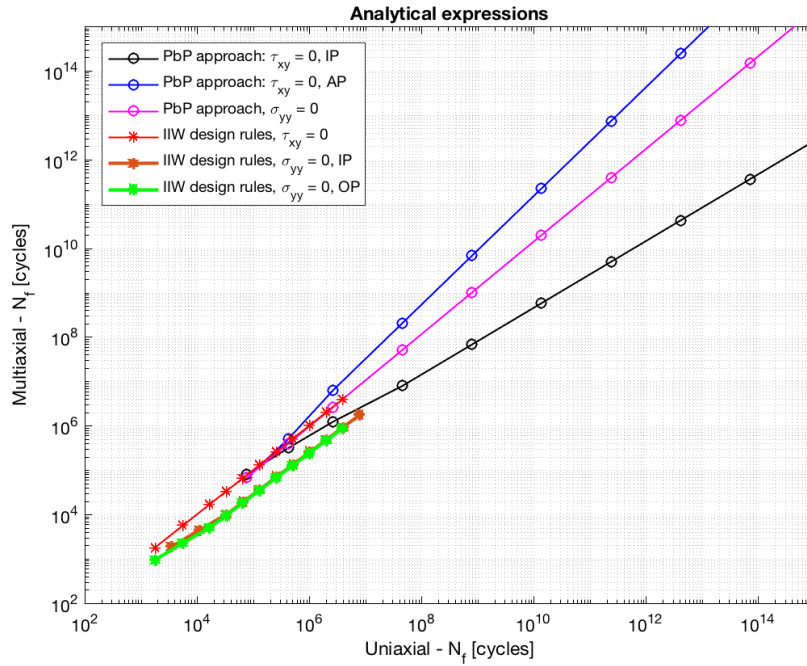


Figure 5.6: Uniaxial damage (in  $N_f$ ) vs. multiaxial damage (in  $N_f$ ) using analytical expressions.

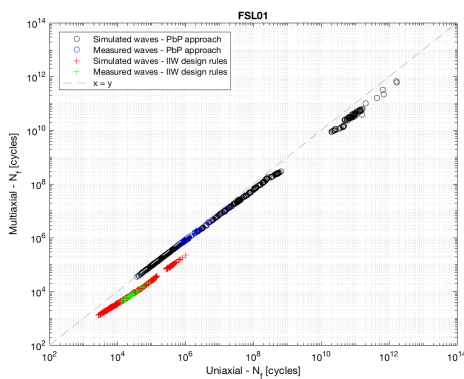


Figure 5.7: Uniaxial damage (in  $N_f$ ) vs. multiaxial damage (in  $N_f$ ) for FSL01 (TF based).

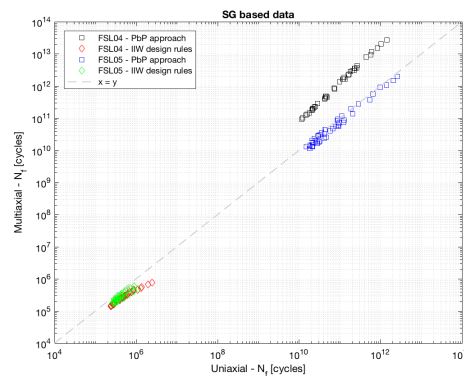


Figure 5.8: Uniaxial damage (in  $N_f$ ) vs. multiaxial damage (in  $N_f$ ) for FSL04 and FSL05 (strain gauge based). Note that the color coding is different from other figures.

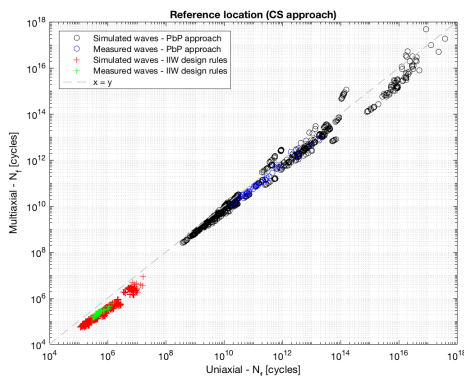


Figure 5.9: Uniaxial damage (in  $N_f$ ) vs. multiaxial damage (in  $N_f$ ) for the reference location using a cold spot approach (TF based).

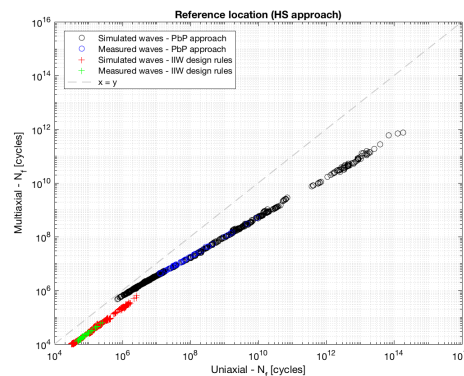


Figure 5.10: Uniaxial damage (in  $N_f$ ) vs. multiaxial damage (in  $N_f$ ) for the reference location using a HS approach (TF based).

a shear SN-curve, resulting in a longer lifetime. The PbP approach implements this using the stress-state estimator  $\rho_{ref}$ , which would be zero if  $\sigma_{xx}(t) = -\sigma_{yy}(t)$  (hydrostatic stress equals 0 at every time  $t$ ). The load path for  $180^\circ$  AP loading is a straight line with slope -1; if this line is projected on the eigenvectors of its own covariance matrix, the result is one projected load path with amplitude equal to the amplitudes of the original load paths  $\sigma_{xx}(t)$  and  $\sigma_{yy}(t)$ . With  $\rho_{ref} = 0$  (shear SN-curve), this results in the fatigue damage as estimated when only considering shear stress. Apparently, the PbP approach takes this physical phenomenon in account correctly, assuming rotation of the plane is always allowed.

In the presence of AP biaxial normal loading (no shear), the value for the stress-state estimator  $\rho_{ref}$  equals zero. As explained, this makes sense since a plane rotated  $45^\circ$  from the AP biaxial normal loading plane contains only shear stresses. What happens when the biaxial loading is IP? The load path is still a straight line, now with slope 1. There is one projected load path with amplitude equal to the amplitude of  $\sigma_{xx}(t)$  and  $\sigma_{yy}(t)$ . The stress-state estimator  $\rho_{ref}$  is now equal to 2. The reference SN-curve is extrapolated from the master SN-curves. Assuming FAT71 and FAT80 as master SN-curves, the reference SN-curve will have a slope of 1. If IP normal stress in  $z$ -direction is also present (with equal amplitude), the slope becomes -1.

The multiaxial fatigue damage is significantly larger when the stress-state is IP (black line), according to the PbP approach. From IIW design rules follows that IP stress-states reduce the fatigue damage. Part of the line where  $\sigma_{yy} = 0$  (pink line) also lies above the line  $x = y$ . This follows directly from the analytical expressions ([52]) and has no physical meaning. The IIW design rules do not take into account loading in transverse direction. It is interesting to note that the IIW design rules can be used directly to estimate the magnitude of the shear loading. When this is known, the PbP approach can be used to estimate the magnitude and phase of the transverse loading.

Based on the above conclusions, FSL01 (Figure 5.7) has a shear component and a relatively small transverse loading component IP with longitudinal loading. The same goes for the SG based data of FSL05 (Figure 5.8 in blue and green) and the reference location using the cold spot approach (Figure 5.9). The reference location using the HS approach has a significantly higher IP transverse loading component. Based on the IIW design rules, a shear component is also present. FSL04 (Figure 5.8 in black and red) has AP transverse loading. Based on the IIW design rules, the shear component is slightly higher than in FSL05. The data in Figures 5.7 - 5.10 is also presented in Appendix D expressed in damage per cycle on a linear scale. This demonstrates the effect at low amount of cycles to failure.

The Stratton data shows a high amount of scatter from  $N_f > 10^{13}$  (Figure 5.5a). This data was not analyzed so the source of the scatter cannot be identified. It is important to observe that the high scatter does not carry over when the focus is shifted to high damage estimates (Figure 5.5b). The same is observed in Figures D.1 - D.4.

The strain gauge data is valuable because it is only dependent of the quality of the strain gauges. Considering the TF based data, the reference location adopting the cold spot approach shows very low fatigue damage. For that reason, it is not included in further analyses.

### 5.3.2. Correlation with wave statistics

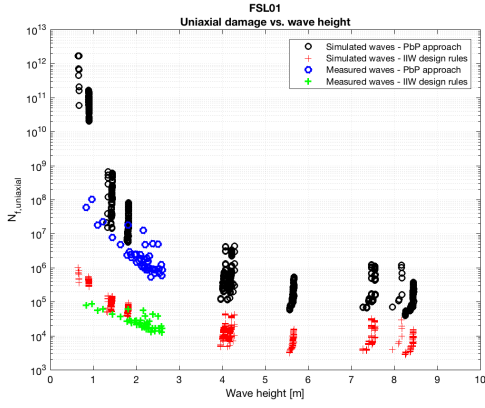
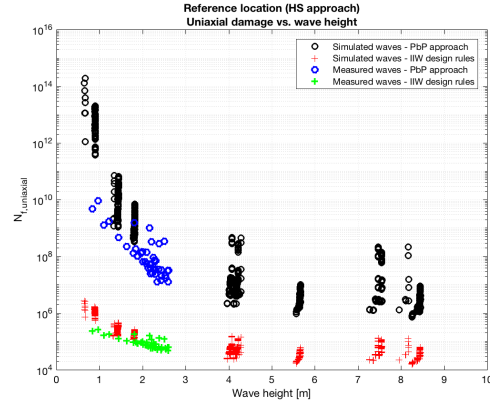
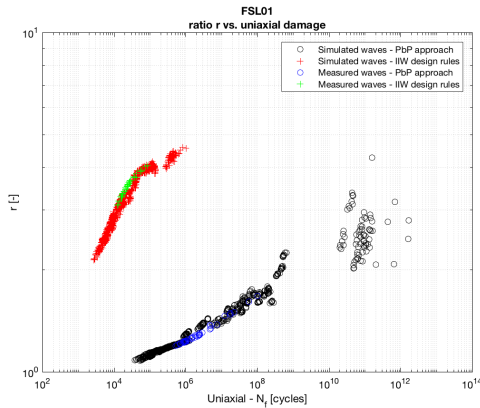
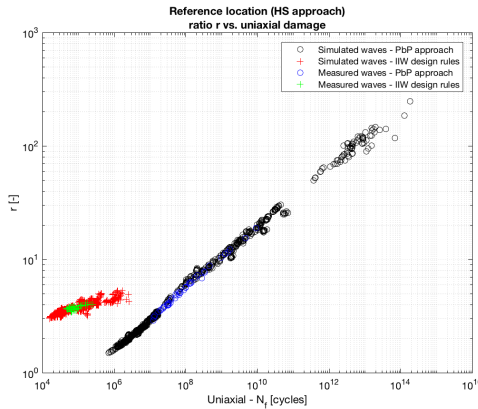
As indicated, this part focuses on FSL01, the reference location using the HS approach, and the strain gauge data. The data is presented as the ratio:

$$r = \frac{N_{f,uniaxial}}{N_{f,multiaxial}} \quad (5.4)$$

i.e.: if this ratio is  $r = 100$ , the uniaxial number of cycles is one hundred times higher than the multiaxial number of cycles to failure. First, the TF based data is presented. Each figure contains four pieces of information:

- Simulated waves, damage calculated using the PbP approach (in black).
- Simulated waves, damage calculated using the IIW design rules (in red).
- Measured waves, damage calculated using the PbP approach (in blue).
- Measured waves, damage calculated using the IIW design rules (in green).

The data collected using the measured waves is included to verify that the simulated waves are representative of a sea-state. The incoming peak wave direction and spreading, and incoming peak wave direction and wave height are uncorrelated. Secondly, the results for the SG based data are presented. These figures contain:

Figure 5.11: FSL01, uniaxial damage (in  $N_f$ ) vs. wave height.Figure 5.12: Reference location (HS approach), uniaxial damage (in  $N_f$ ) vs. wave height.Figure 5.13: FSL01, ratio  $r$  vs. uniaxial damage (in  $N_f$ ).Figure 5.14: Reference location (HS approach), ratio  $r$  vs. uniaxial damage (in  $N_f$ ).

- FSL04, damage calculated using the PbP approach (in black).
- FSL04, damage calculated using the IIW design rules (in red).
- FSL05, damage calculated using the PbP approach (in blue).
- FSL04, damage calculated using the IIW design rules (in green).

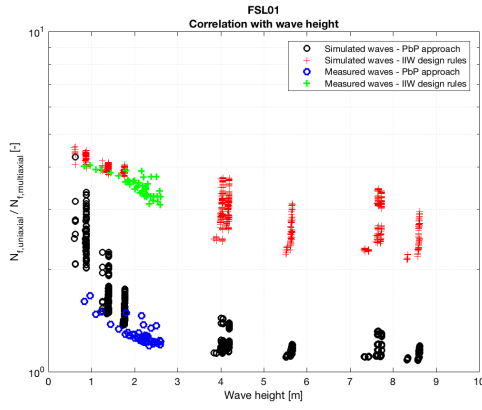
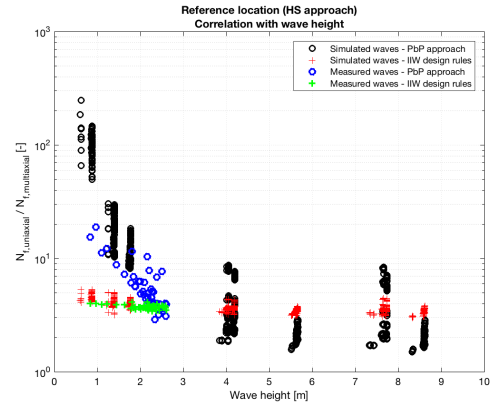
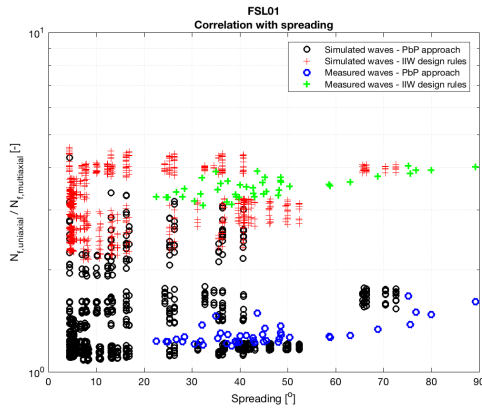
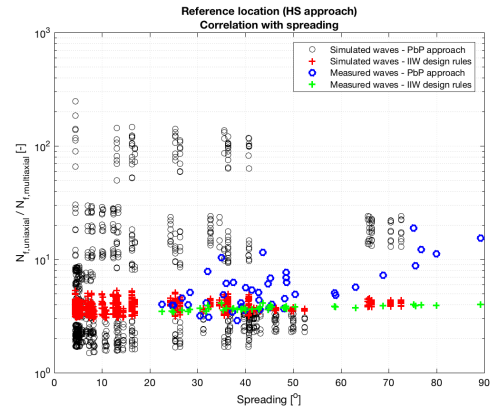
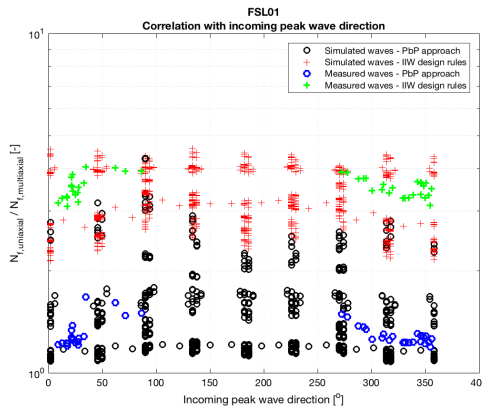
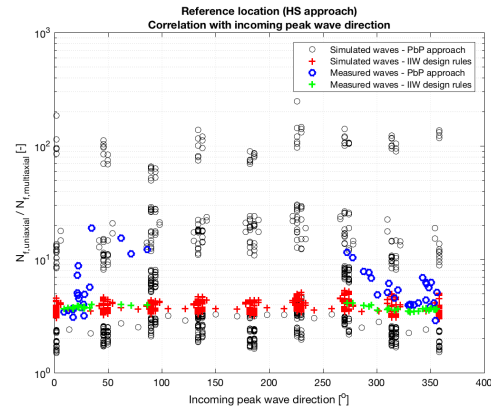
Note that this color coding is different from previous figures. This data can only be correlated to measured wave data.

### Results

For future reference, the uniaxial damage (expressed in  $N_f$ ) is plotted against the wave height in Figures 5.11 (FSL01) and 5.12 (reference location), and the ratio  $r$  (Equation 5.4) is plotted against the uniaxial number of cycles to failure in Figures 5.13 (FSL01) and 5.14 (reference location). The correlation for the TF based data between the ratio  $r$  and the wave height for FSLO1 is depicted in Figure 5.15 and for the reference location in Figure 5.16, the spreading for FSLO1 in Figure 5.17 and the for reference location in Figure 5.18, the incoming peak wave direction for FSLO1 in Figure 5.19 and for the reference location in Figure 5.20. The correlation for the SG based data between the ratio  $r$  defined above and the wave height is depicted in Figure 5.21, the spreading in Figure 5.22 and the incoming peak wave direction in Figure 5.23.

### Considerations

The damage estimates obtained using the simulated wave data seems to agree well with the damage estimates obtained using the measured wave data, with the exception of very low waves. This fact was already addressed in Chapter 4 and related to the white noise.

Figure 5.15: FSL01, correlation damage (in  $N_f$ ) and wave height.Figure 5.16: Reference location (HS approach), correlation damage (in  $N_f$ ) and wave height.Figure 5.17: FSL01, correlation damage (in  $N_f$ ) and spreading.Figure 5.18: Reference location (HS approach), correlation damage (in  $N_f$ ) and spreading.Figure 5.19: FSL01, correlation damage (in  $N_f$ ) and the incoming peak wave direction.Figure 5.20: Reference location (HS approach), correlation damage (in  $N_f$ ) and the incoming peak wave direction.

In Figures 5.15 and 5.16, the spreading in the ratio  $r$  seems to be smaller at a wave height of about  $5.5m$  than at surrounding wave heights. The same trend is observed in Figures 5.11 and 5.12 where the uniaxial number of cycles to failure is related to the wave height. This wave height corresponds to a peak frequency of  $0.5rad/s$  or peak period of about  $12.6s$ . At this frequency, the maximum forced torsion response is expected. The torsion response inevitably included normal stresses due to warping. This results in higher damage estimates.

The ratio  $r$  has its lowest values at head and following waves (Figures 5.19 and 5.20), which makes sense considering that the response is dominated by longitudinal bending. It would make sense that the spreading

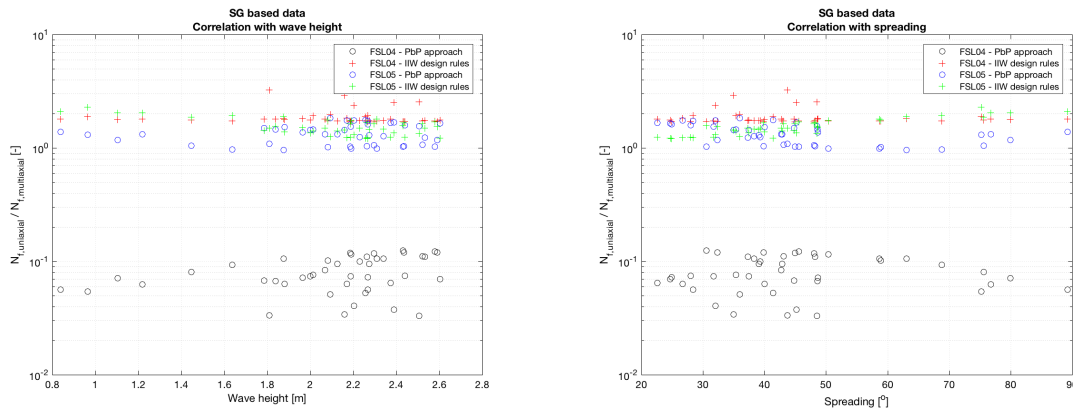


Figure 5.21: Strain gauge data, correlation damage (in  $N_f$ ) and wave height. Figure 5.22: Strain gauge data, correlation damage (in  $N_f$ ) and spreading.

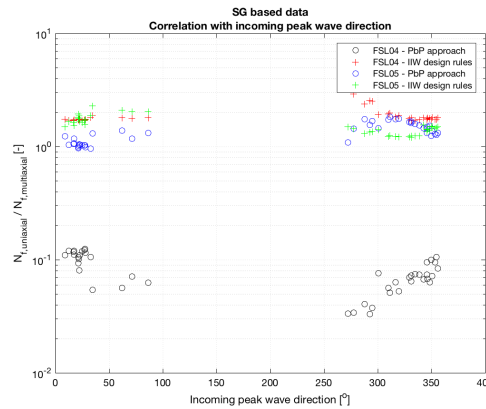


Figure 5.23: Strain gauge data, correlation damage (in  $N_f$ ) and the incoming peak wave direction.

in the ratio  $r$  would be low when the response is dominated by longitudinal bending, but this is not observed. This (amongst other things) is discussed in the next section.

### 5.4. Discussion

The methods used to estimate fatigue damage are the IIW design rules and the (modified) PbP approach. If only one method were used, it would be difficult to distinguish methodological properties from physical phenomena. Methodological properties were investigated in Figure 5.6. This figure shows that the IIW design rules provide a much more simplistic and conservative damage estimate. The IIW design rules do not take into account transverse loading. However, expected lifetime estimates (in  $N_f$ ) are significantly lower than the PbP estimates. The PbP approach includes phase angles in longitudinal and transverse loading, and distinguishes between IP, OP and AP loading. Note that it was already concluded in Chapter 3 that the applicability of the linearly inter- and extrapolated SN-curves is limited to  $N_f > 2 \cdot 10^4$ , based on what was investigated. One of the mathematical properties of the PbP approach is that the multiaxial damage becomes lower than uniaxial damage when biaxial loading comprised of shear and normal loading is assumed. The intersection point where uniaxial damage equals multiaxial damage depends on the magnitudes of the shear and normal loading. This intersection point occurs at a lower amount of cycles to failure when less shear stress is present. When more shear stress is present, the intersection point occurs at a higher amount of cycles to failure.

It is observed that, for both employed methods, there seems to be strong correlation between the wave height and the ratio uniaxial number of cycles to failure over multiaxial number of cycles to failure. This fact is also proved using the analytical expressions. It is observed from Figure 5.6 that the presence of multiaxial stress-states (generally) results in a slope change when the uniaxial number of cycles is plotted against the multiaxial amount of cycles, the only exception being when the slope induced by IP loading in transverse direction is countered by the slope change induced by shear loading. Since this data is plotted on a log-log

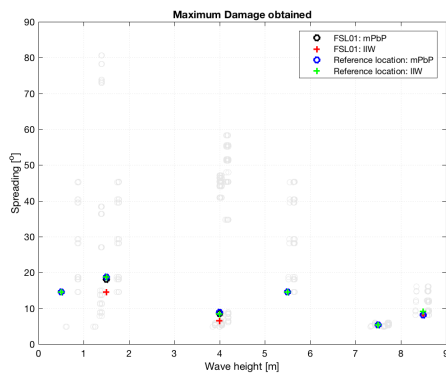
scale, a slope change results in an exponential growth or decay of the ratio uniaxial number of cycles to failure over multiaxial number of cycles to failure. Growth is present when the slope is lower than 1 (black line Figure 5.6), decay when the slope is higher than 1 (blue line Figure 5.6). Additionally, the presence of multiaxial stress-states due to the structural response not being dominated by global bending results in shorter lifetime estimates in low wave heights.

For every wave height, some spreading in the ratio  $r$  is observed. It is investigated at which spreading and incoming peak wave direction the highest ratio  $r$  for a discrete set of wave heights is found. For reference, the same is done for damage. The results are depicted in Figure 5.24 for the damage and Figure 5.25 for the ratio  $r$ . The results in Figure 5.24 are true for both multiaxial and uniaxial fatigue estimates.

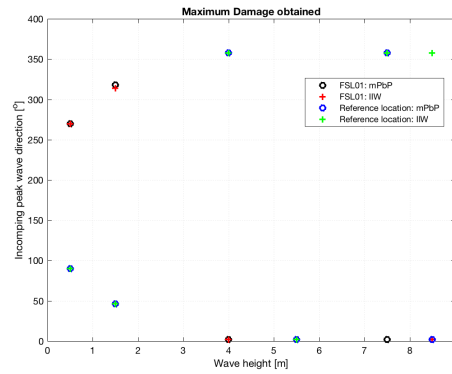
It is observed that the maximum damage is obtained at incoming peak wave directions of  $90^\circ$  and  $270^\circ$  (beam waves) for wave heights of about  $0.5m$ , and  $0^\circ$  and  $360^\circ$  (head waves) for wave heights higher than  $3m$ . This suggests that the presence of multiaxial stress-states is more relevant at low wave heights. These results suggest that, at lower wave heights, the torsion response results in significant magnification of the fatigue damage. The maximum ratio  $r$  at low wave heights is obtained at beam, bow and quartering waves. The maximum ratio  $r$  at high waves is obtained at beam waves. From this is concluded that the maximum ratio  $r$  at high waves is found due to a lack of global bending. In low waves, the maximum ratio  $r$  is found due to the presence of multiaxial stress-states. This explains why the spreading in the  $r$  ratio is not necessarily small when head or following waves are considered. Both maximum damage estimates and maximum ratios are found at low spreading, suggesting that both are governed by the incoming peak wave direction. The only exception is found in the maximum obtained ratio at a wave height of  $5.5m$ . It was concluded earlier that at this wave height the maximum torsion response is expected. It is expected that in this sea-state, a confused sea-state consisting of head and bow waves results in the maximum ratio  $r$ .

The maximum ratio  $r$  as a function of wave height is depicted in 5.26. Since it has been concluded that the maximum ratio is obtained at wave characteristics that result in low damage estimates, it is investigated what the ratio is in wave characteristics that result in the highest damage, as a function of wave height (see Figure 5.24b and Figure 5.24a). These results are depicted in 5.27.



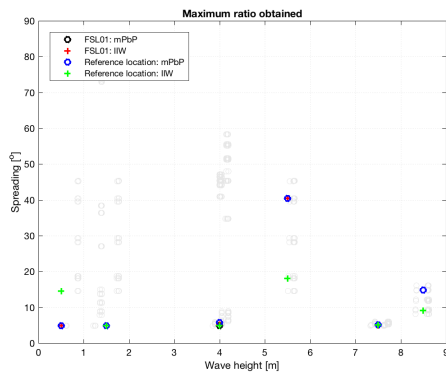


(a) Damage estimate (in  $N_f$ ) vs. spreading.

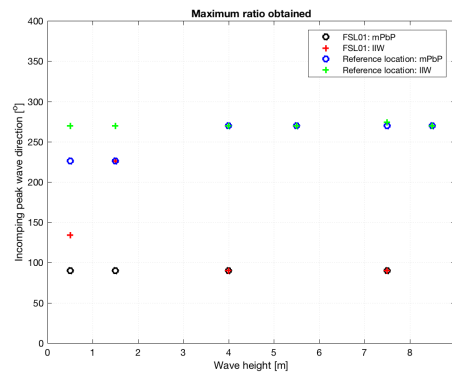


(b) Damage estimate (in  $N_f$ ) vs. incoming peak wave direction.

Figure 5.24: Maximum damage obtained for a discrete set of wave heights as a function of spreading and incoming wave direction. The spreading as a function of the wave height for all simulated waves is added in light grey.



(a) ratio  $r$  vs. spreading.



(b) ratio  $r$  vs. incoming peak wave direction.

Figure 5.25: Maximum ratio  $r$  obtained for a discrete set of wave heights as a function of spreading and incoming wave direction. The spreading as a function of the wave height for all simulated waves is added in light grey.

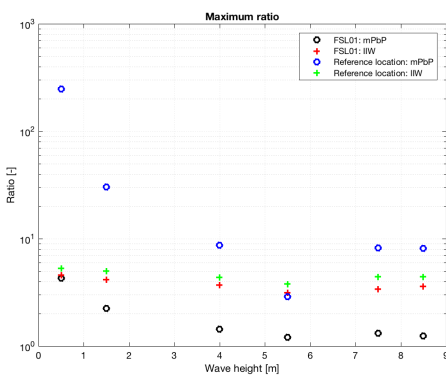


Figure 5.26: Maximum ratio  $r$ .

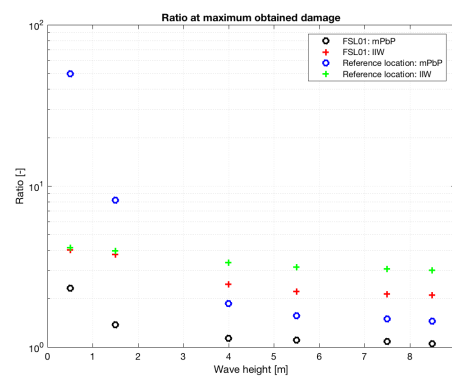


Figure 5.27: Ratio  $r$  in wave characteristics that result in the highest damage estimates.



# 6

## Conclusion and recommendation

*"I think you should always bear in mind that entropy is not on your side" – Elon Musk*

---

### 6.1. Conclusions

The effect of multiaxial stress-states on fatigue damage in frigate type structures was investigated. In order to do so, an existing model - the Projection-by-Projection approach - was implemented and tested for its applicability to welded joints in frigate type structures. The analysis utilized a combination of measured data (from strain gauges) and transfer function in combination with wave data. Wave data was available from the WaMoS Wave Radar aboard the USCG Cutter Bertholf. Additionally, 3-D wave spectra were modeled based on the Global Wave Statistics. Fatigue damage estimates were calculated using the IIW design rules and PbP approach. Based on the results, the following conclusions can be drawn:

- The stress-state may become almost entirely proportional due to geometry changes, as observed in FSL01. Anti-phase stress-states are observed in FSL04. The reference location shows that the stress-state proportionality depends on incoming wave direction and wave height (thus: peak frequency). It can be concluded that stress-state proportionality varies between fully fully proportional (IP or AP) and fully non-proportional (OP), depending on the type of detail, location in the vessel and wave characteristics.
  - The IIW design rules state that OP loading increases the fatigue damage because of the varying principal stress direction. For this reason, no distinguish is made between IP and AP loading (in both cases, the principal stress direction does not change). The PbP approach does not account for phase shifts in shear loading. The PbP approach returns the highest damage estimates when the transverse loading is IP and smallest when it is AP.
- Scenarios where the ratio uniaxial number of cycles to failure over multiaxial number of cycles to failure exceeds one hundred have been observed. However, this only happens when the damage estimates are extremely low. Considering the PbP approach, this ratio is  $r = 1.85$  for the reference location (adopting a HS approach) and  $r = 1.3$  for FSL01, both at  $N_f = 2 \cdot 10^6$ . When the IIW design rules are considered, these ratios are approximately equal at  $r = 4.5$ .
  - This suggests that the ratio  $S_{xx}/S_{xy}$  - where  $S_{xx}$  is the amplitude of  $\sigma_{xx}$  and  $S_{xy}$  is the amplitude  $\tau_{xy}$  - is approximately equal for FSL01 and the reference location (IIW returns the same ratio). However, The reference location has a higher IP loading in transverse direction, resulting in significantly higher damage estimates by the PbP approach.
  - Data that was not investigated in depth was from FSL04 and FSL05 (not enough data), and from the reference location. The damage estimates from these locations were too low to draw valuable conclusions. On average, multiaxial damage was 1.3 times higher than uniaxial damage for FSL05

and 1.5 times higher for the reference location (cold spot) when the damage per cycle is considered. FSL04 showed uniaxial damage estimates that were 7 times higher than multiaxial damage due to the presence of an AP stress-state.

- Multiaxial stress-states have the highest influence at beam waves, where the global bending response is the lowest. When the influence of the multiaxial stress-states is considered in conditions that are least favorable with respect to fatigue damage, the influence is much lower.
- The maximum multiaxial damage and uniaxial damage were found in the same sea-states. From this can be concluded that the longitudinal stress remains governing, even when multiaxial stress-states are considered.
- Only considering loading in longitudinal direction could be a non-conservative approach (it was argued that AP biaxial normal loading (no shear stress) is the same as a shear stress with equal amplitude on a  $45^\circ$  rotated plane). However, this is not a realistic stress-state in frigate type structures; it is expected that this will not influence fatigue damage calculations significantly.
- The ratio uniaxial number of cycles to failure over multiaxial number of cycles to failure is highest at low wave heights. This is both a result of the mathematics of the methods - since it followed from the analytical results - as well as physical properties.
  - The presence of multiaxial stress-states is governed by the incoming peak wave direction. For waves with a significant wave height  $H_S > 3$ , multiaxial stress-states are most relevant when there is little global bending. For waves with a significant wave height  $H_S < 2$ , bow and quartering waves result in a significant magnification of the fatigue damage.
  - Considering that multiaxiality is most relevant for low damage estimates, this raises the question whether multiaxiality is important on a macroscopic time scale. Most of the time, a vessel will be sailing through mild to moderate sea-states where multiaxiality may play a role. It might be so, that the sea-states with higher wave heights that occur only a small percentage of the time are governing with regards to fatigue damage. In these sea-states, multiaxiality is of small influence.
- The Stratton data shows a high amount of scatter at low damage estimates. Since the data is not investigated, the source of this scatter cannot be determined. It is known that this scatter can be produced by stress-state non-proportionality. This suggests that the proportionality in this particular detail is fully dependent of the incoming wave direction and wave height. However, this cannot be proven. When the damage per cycle is considered, the multiaxial damage is a factor 2.2 higher than the uniaxial damage (on average).

## 6.2. Recommendation

The validity of this study is dependent of some influence factors. These influence factors and recommended future research will be discussed here.

### *Validity of the FE model used to obtain the transfer functions*

The validity of the FE model could not be investigated in this research. Transfer functions were only available at one location in the vessel that was instrumented with a unidirectional strain gauge: FSL01. This means that only stresses in longitudinal direction could be validated. Furthermore, transfer functions were only available for 7 wave directions and a vessel speed of  $16 \text{ knots}$ . At this velocity, the accuracy of the transfer functions is limited to the accuracy of the potential theory. A reliable validation of the FE model would require more information; a methodology to validate the FE model is included in Appendix E.

### *Validity of the models used to estimate fatigue damage*

The validity of the results is extremely dependent of the validity of the models used to estimate fatigue damage. The applicability of the PbP approach has been thoroughly investigated and some modifications were made that improve the behavior of the approach. It was found that the applicability is limited to certain conditions. Additionally, fatigue damage was also estimated using the IIW design rules. Even though a comparative study was performed in [54], there is no consensus yet on which method best estimates fatigue damage in the presence of non-proportional variable amplitude loading. More research is required.

*The influence of the mean stress on fatigue damage*

Still water pressures, cargo loads and other (quasi-) static loads result in static bending moments and forces in structural members. The influence of the mean stress was not included in this research since the employed methods did either not account for them (IIW design rules), or no suitable method to account for mean stress was found (PbP approach). Suitable in this context means that no evidence was present that the proposed models to account for mean stress in combination with the PbP approach was correct. Two models to account for mean stress were proposed in Chapter 3, the Walker correction was preferred. Research is necessary to validate this correction in combination with the PbP approach.

*Sea-state occurrence*

This study did not include probability of occurrence of sea-states. The results present the sea-states that is least favorable when multiaxial fatigue damage is considered. The results have to be combined with a scatter diagram, that includes spreading and incoming wave direction, to determine the overall influence of multiaxial fatigue damage on the expected fatigue lifetime.



# Bibliography

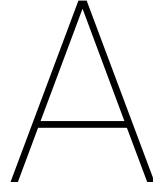
- [1] Ansys apdl, release 17.1. *Element Reference*. ansys, inc.
- [2] URL [https://en.wikipedia.org/wiki/Fracture\\_mechanics](https://en.wikipedia.org/wiki/Fracture_mechanics).
- [3] . URL <http://www.marin.nl/web/JIPs-Networks/Archive-JIPs-public/Valid.htm>.
- [4] . URL <http://www.marin.nl/web/JIPs-Networks/JIPs-public/VALID-II.htm>.
- [5] . URL <http://www.sea-image.com>.
- [6] *Water Wave Propagation Over Uneven Bottoms: Linear wave propagation*. World Scientific, 1997.
- [7] *Recommendations for Fatigue Design of Welded Joints and Components*. Springer Science+Business Media, B.V., 2016.
- [8] I.V. Papadopoulos; P. Davoli; C. Gorla; M. Filippini; A. Bernasconi. *A comparative study of multiaxial high-cycle fatigue criteria for metals*. *International Journal of Fatigue*, 1997.
- [9] L.E. Borgman. *Statistical Models for Ocean Waves and Wave Forces*. *Advances in Hydroscience*, 1969.
- [10] C.H. Wang; M.W. Brown. *A Path-Independent Parameter for Fatigue Under Proportional and Non-Proportional Loading*. *Fatigue & Fracture of Engineering Materials & Structures*, 1993.
- [11] B. Cotterell. *Notes on Paths and Stability of Cracks*. *International Journal of Fracture Mechanics*, 1966.
- [12] K. Dang-Van. *Macro-Micro Approach in High-Cycle Multiaxial Fatigue*. *Advances in Multiaxial Fatigue*, 1993.
- [13] J.H. den Besten. *Fatigue resistance of welded joints in aluminium high-speed craft: A TOTAL STRESS CONCEPT*. PhD thesis, Delft University of Technology, 2015.
- [14] J.H. den Besten. *Lecture notes in fatigue and fracture in marine structures*, 2016.
- [15] M.St. Denis. *On the Motions of Ships in Confused Seas*. SNAME Transactions, 1953.
- [16] F.P. Beer; E.W. Johnston; J.T. DeWolf. *Mohr circles, stress paths and geotechnics*. McGraw Hill, 1992.
- [17] *Fatigue design of offshore steel structures*. DNV-GL, April 2016.
- [18] J. Mei; P. Dong. *A new path-dependent fatigue damage model for non-proportional multi-axial loading*. *International Journal of Fatigue*, 2016.
- [19] P. Dong. *A robust structural stress method for fatigue analysis of ship structures*. Technical report, Center for Welded Structures Research, 2003.
- [20] N.E. Dowling. *Mean Stress Effects in Stress-Life and Strain-Life Fatigue*. Technical report, Virginia Polytechnic Institute and State University, 2004.
- [21] M. Matsuishi; T. Endo. *Fatigue of metals subjected to varying stress*. Technical report, Japan Society of Mechanical Engineers, 1968.
- [22] W.N. Findley. *A Theory for the Effect of Mean Stress on Fatigue of Metals Under Combined Torsion and Axial Load or Bending*. *Journal of Engineering for Industry*, 1959.
- [23] B. Li; J.L. Santos; M. De Freitas. *A unified numerical approach for multiaxial fatigue limit evaluation*. *Mechanics of Structures and Machines*, 2000.
- [24] S. Timoshenko; J.J. Goodier. *Theory of Elasticity*. McGraw Hill, 1987.

- [25] J. Goodman. *Mechanics Applied to Engineering*. Longman, Green & Company, 1899.
- [26] K.A. Stambaugh; I. Drummen; C. Cleary; R. Sheinberg; M.L. Kaminski. *Structural Fatigue Life Assessment and Sustainment Implications for a New Class of US Coast Guard Cutters*. Technical report, USCG, 2014.
- [27] P. Aalberts; M. Kaminski. *Full Scale Instrumentation Plan*, 2008.
- [28] G. Labeas; T. Kermanidis. *Stress multiaxiality factor for crack growth prediction using the strain energy density theory*. Technical report, University of Patras, 2006.
- [29] D.F. Socie; P. Kurath; J. Koch. *A Multiaxial Fatigue damage paramter. Biaxial and Multiaxial Fatigue*, 1989.
- [30] C.M. Sonsino; M. Kueppers. *Multiaxial fatigue of welded joints under constant and variable amplitude loadings. Fatigue & Fracture of Engineering Materials & Structures*, 2001.
- [31] A. Fatemi; I. Yang. *Cumulative fatigue damage and life prediction theories; a survey of the state of the art for homogeneous materials. International Journal of Fatigue*, 1998.
- [32] L. Susmel; P. Lazzarin. *A bi-parametric Wohler curve for high cycle multiaxial fatigue assessment. Fatigue & Fracture of Engineering Materials & Structures*, 2002.
- [33] L. Susmel; R. Tovo; P. Lazzarin. *The mean stress effect on the high-cycle fatigue strength from a multiaxial fatigue point of view. International Journal of Fatigue*, 2004.
- [34] W.T. Lee. *Global Wave Statistics for Structural Design Assessments*. Technical report, Naval Surface Warfare Center, 1995.
- [35] R.H. Legatt. *Residual stresses in welded structures. International Journal of Pressure Vessels and Piping*, 2008.
- [36] C. Van Loan. *Computational Frameworks for the Fast Fourier Transform*. Society for Industrial and Applied Mathematics, 1992.
- [37] R. A. Sousa; J.T.P. Castro; A.A.O. Lopes; L.F. Martha. *On improved crack tip plastic zone estimates based on T-stress and on complete stress fields. Fatigue & Fracture of Engineering Materials & Structures*, 2012.
- [38] P.P. Milella. *Fatigue and Corrosion in Metals*. Springer Science+Business Media, B.V., 2012.
- [39] N.I. Muskhelishvili. *Some Basic Problems of the Mathematical Theory of Elasticity*. Noordhoff, 1963.
- [40] U.S. Department of Homeland Security. *Budget-in-brief*, 2009.
- [41] J.L. Hanson; O.M. Phillips. *Wind Sea Growth and Dissipation in the Open Ocean. Journal of Physical Oceanography*, 1999.
- [42] R.E.D. Bishop; W.G. Price. *Hydroelasticity of Ships*. Cambridge University Press, 1979.
- [43] J. Schijve. *Fatigue of Structures and Materials*. Springer Science+Business Media, B.V., 2009.
- [44] P.J.G. Schreurs. *Fracture Mechanics*. Eindhoven University of Technology, 2012.
- [45] A. Fatemi; N. Shamsaei. *Multiaxial fatigue: An overview and some approximation models for life estimation. International Journal of Fatigue*, 2011.
- [46] S. Suresh. *Fatigue of Materials*. Cambridge University Press, 1998.
- [47] P. Lazzarin; L. Susmel. *A stress-based method to predict lifetime under multiaxial fatigue loadings. Fatigue & Fracture of Engineering Materials & Structures*, 2003.
- [48] Y. Wang; L. Susmel. *Critical plane approach to multiaxial variable amplitude fatigue loading*. Technical report, Nanjing University of Aeronautics and Astronautics, 2015.
- [49] I. Thompson. *Validation of naval vessel spectral fatigue analysis using full- scale measurements. Marine Structures*, 2016.



- 
- [50] E. Thornhill. *Real Time Local Sea State Measurement Using Wave Radar and Ship Motions*. Technical report, SNAME Transaction, 2010.
- [51] A. Cristofori; D. Benasciutti; R. Tovo. *A stress invariant based spectral method to estimate fatigue life under multiaxial random loading*. Technical report, University of Ferrara, 2011.
- [52] A. Cristofori; L. Susmel; R. Tovo. *A stress invariant based criterion to estimate fatigue damage under multiaxial loading*. Technical report, University of Ferrara, 2007.
- [53] D. Benasciutti; R. Tovo. *Cycle distribution and fatigue damage assessment in broad-band non-Gaussian random processes*. *Probabilistic Engineering Mechanics*, 2005.
- [54] P.S. van Lieshout; J.H. den Besten; M.L. Kaminski. *Comparative study of multiaxial fatigue methods applied to welded joints in marine structures*. Technical report, Delft University of Technology, 2016.
- [55] K.A. Stambaugh; Jr. P.R. van Mater. *Fatigue performance under multiaxial loading in marine structures*. Technical report, Ship Structure Committee, 1990.
- [56] T.E. Langlais; J.H. Vogel. *Multiaxial cycle counting for plane method*. *International Journal of Fatigue*, 2003.
- [57] K. Walkere. *The Effect of Stress Ratio During Crack Propagation and Fatigue for 2024-t3 and 7075-t6 Aluminum*. Defense Technical Information Center, 1970.
- [58] D. Wang. *Three-Dimensional Hydroelastic Analysis of Ships in Time Domain*. PhD thesis, China Ship Scientific Research Centre, 1996.
- [59] Y. Wu. *Hydroelasticity of Floating Bodies*. PhD thesis, Brunel University, 1984.





# Characteristic equation, invariants and the definition of stress quantities

In linear algebra, an eigenvector of a linear transformation is a non-zero vector that does not change its direction when the linear transformation is applied. This can be written as the following equation:

$$\mathbf{A}v = \lambda v \quad (\text{A.1})$$

where  $\mathbf{A}$  is an  $n$  by  $n$  square matrix,  $v$  is a  $n$  by 1 column vector and  $\lambda$  is a scalar, known as the eigenvalue. Equation A.1 can be rewritten as:

$$(\mathbf{A} - \lambda \mathbf{I})v = 0 \quad (\text{A.2})$$

Equation A.2 has a non-trivial solution if and only if the determinant of  $\mathbf{A} - \lambda \mathbf{I}$  is 0. The eigenvalues of  $\mathbf{A}$  are those values of  $\lambda$  that satisfy the equation

$$\det(\mathbf{A} - \lambda \mathbf{I}) = 0 \quad (\text{A.3})$$

The resulting equation is  $n^{\text{th}}$  order polynomial, whose solutions are the eigenvalues. For a 3x3 matrix, the solution of Equation A.3 is:

$$\det(\mathbf{A} - \lambda \mathbf{I}) = -\lambda^3 + J_1\lambda^2 - J_2\lambda + J_3 = 0 \quad (\text{A.4})$$

where  $\{J_1, J_2, J_3\}$  are the invariants and all solutions of  $\lambda$  are the eigenvalues. Equation A.4 is known as the characteristic equation. The eigenvectors are found by substituting the eigenvalues in Equation A.2 and solving for  $v$ .

A 3-dimensional element has 6 stress components (3 normal components and 3 shear components). Using the definitions in Equations 3.1 and 3.2, it can quite easily be verified that the second invariant  $J_2$  can be written, in terms of the deviatoric stress, as [8]:

$$J_2 = \frac{3}{4}\sigma'_{xx}{}^2 + \frac{1}{4}(\sigma'_{yy}{}^2 - \sigma'_{zz}{}^2)^2 - \frac{1}{2}\sigma'_{yy}\sigma'_{zz} + \sigma'_{xy}{}^2 + \sigma'_{xz}{}^2 + \sigma'_{yz}{}^2 \quad (\text{A.5})$$

or, equivalently, as the length of the vector  $s$ :

$$s = \left[ \frac{\sqrt{3}}{2}\sigma'_{xx}; \frac{1}{2}(\sigma'_{yy} - \sigma'_{zz}); \sigma'_{xy}; \sigma'_{xz}; \sigma'_{yz} \right] \quad (\text{A.6})$$

When all stress components are time-dependent, the vector  $s$  becomes time-dependent as well. The tip of the vector  $s(t)$  is denoted as the load path.



# B

## Wave characteristics

The spreading parameter is defined to capture multiple wave properties in one parameter, such that this parameter can be correlated with properties of the multiaxial fatigue damage. A typical 3-D wave spectrum is included in Figure B.1. The energy per wave direction  $E_\theta(\theta)$  is obtained by integrating this 3-D spectrum over the frequencies. This is depicted in Figure B.2. The incoming peak wave direction is defined as the wave direction where  $E_\theta(\theta)$  has a maximum.

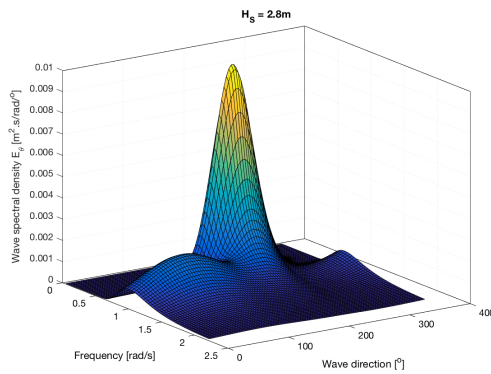


Figure B.1: A typical 3-D wave spectrum.

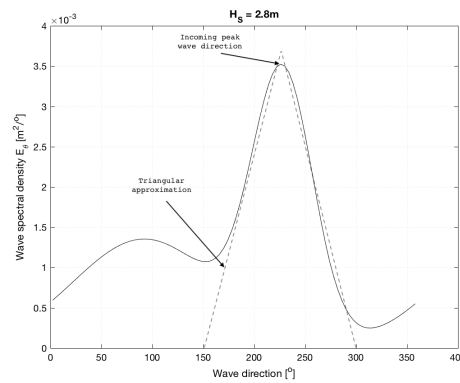


Figure B.2: Energy per wave direction  $E_\theta(\theta)$ .

The energy per wave spectrum can be modeled by two triangles. These triangles have a height  $h$  and a base  $b$ . Since the spreading does not influence the wave height, the area under these triangles must always be constant. This means that:

$$\frac{1}{2}bh = C \quad (B.1)$$

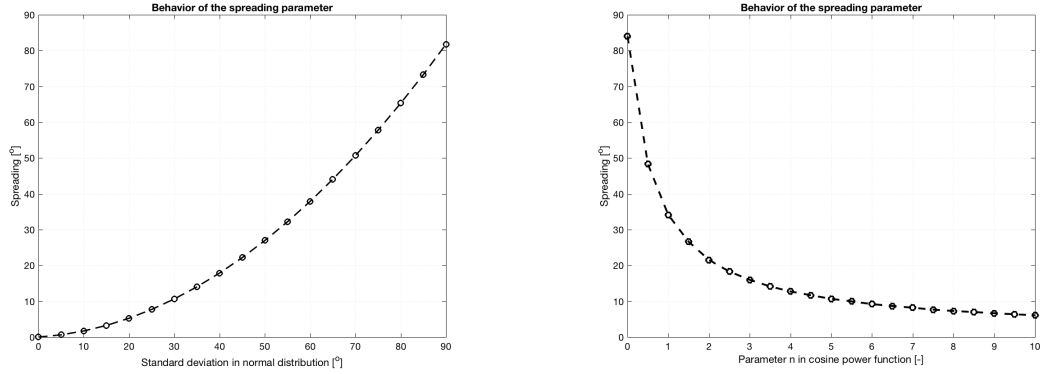
and thus

$$h = 2\frac{C}{b} \quad (B.2)$$

where the constant  $C$  is a measure for the wave height squared. Half the base is defined as the spreading  $Spr_i$  of a particular wave type, where  $i$  represents either wind or swell waves. Let the small triangle be the wind wave and the large triangle be the swell wave. All wave properties can be described by the peak direction of a wave  $\theta_i$ , the constant  $C_i$  and the spreading. The spreading parameter of the total 3-D spectrum  $\theta_{spr}$  is defined as:

$$\theta_{spr} = 2 \cdot \frac{\int_{\theta_I-180}^{\theta_I} (\theta_I - \theta) \cdot E_\theta(\theta) d\theta + \int_{\theta_I}^{\theta_I+180} (\theta - \theta_I) \cdot E_\theta(\theta) d\theta}{360 \cdot \max E_\theta(\theta)} \quad (B.3)$$

With the wave modeled as triangles, this formula can be reduced to an analytical expression for the wave spreading parameter  $\theta_{spr}$ :



(a) The spreading parameter for waves modeled by a normal distribution. (b) The spreading parameter for waves modeled by a cosine-power function.

Figure B.3: Behavior of the spreading parameter in Equation B.3 for wave spreading modeled by two different wave spreading functions.

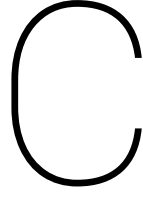
$$\theta_{spr} = \frac{1}{6} \frac{C_{swell} Spr_{swell}^2 + 6C_{wind} Spr_{swell} \cdot |\theta_{swell} - \theta_{wind}|}{C_{swell}} \quad (\text{B.4})$$

The maximum value for the wave spreading is  $180^\circ$ . It is important to note that this analytical expression is only partly true. The numerator in Equation B.3 is split up into two parts. This is because a difference in wave direction between swell and waves cannot be higher than  $180^\circ$ ; an incoming wave of  $360^\circ$  equals an incoming wave of  $0^\circ$ . In Equation B.4 is assumed that both triangles fall within a  $180^\circ$  range.

Important things to note are that the spreading parameter  $\theta_{spr}$  decays exponentially with  $C_{swell}$ , grows linearly with the  $C_{wind}$  and the difference between the incoming wave directions  $\theta_{swell}$  and  $\theta_{wind}$  and grows parabolically with the spreading of the swell  $Spr_{swell}$ . Together with the wave height, which is a function of  $C_{swell}$  and  $C_{wind}$ , and the incoming peak wave direction, this parameter gives a good representation of the sea-state.

The waves were modeled according to a normal distribution. If a single wave component is considered, this parameter provides a measure for the wave spreading. To quantify the behavior, the spreading as calculated using Equation B.3 is calculated for waves modeled using a normal distribution with different values of the standard deviation. The result is depicted in Figure B.3a. For reference, the spreading parameter is also plotted against the parameter  $n$  in the cosine-power spreading function in Figure B.3b. The cosine-power function is [15]:

$$D(\theta) = \frac{\Gamma(n+1)}{\sqrt{\pi}\Gamma(s+\frac{1}{2})} \cos^{2n}(\theta - \theta_I) \quad (\text{B.5})$$



## Structural stress method

### Hot spot stress estimation

This method can be found in [19]. For a continuous weld, the elements along the weld toe are used to extract the nodal forces. For linear shell/plate elements, the work done by the nodal forces over the nodal displacements is equal to the work done by the line forces over the same nodal displacements. The equivalent line forces can be calculated from a system of linear equations in matrix form:

$$\begin{Bmatrix} F_1 \\ F_2 \\ F_3 \\ \vdots \\ F_n \end{Bmatrix} = \begin{bmatrix} \frac{l_1}{3} & \frac{l_1}{6} & 0 & 0 & \cdots \\ \frac{l_1}{6} & \frac{l_1+l_2}{3} & \frac{l_2}{6} & 0 & \cdots \\ 0 & \frac{l_2}{6} & \frac{l_2+l_3}{3} & \frac{l_3}{6} & \cdots \\ \vdots & \vdots & \vdots & \vdots & \ddots \end{bmatrix} \begin{Bmatrix} f_1 \\ f_2 \\ f_3 \\ \vdots \\ f_n \end{Bmatrix} \quad (\text{C.1})$$

In this equation,  $f_1, f_2, \dots, f_n$  are line forces and  $l_i$  are represents the element edge length (a constant for all  $i$  if the element size is equal for all elements). Equivalently, the line moments can be calculated by substituting  $M_1, M_2, \dots, M_n$  for  $F_1, F_2, \dots, F_n$  in the above equation. The structural stress at each node can be calculated as:

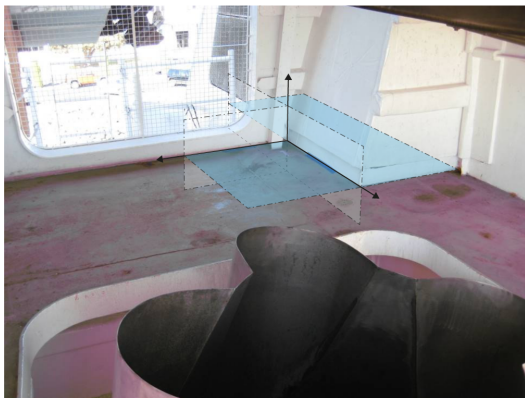
$$\sigma_{s,i} = \sigma_{m,i} + \sigma_{b,i} = \frac{f_i}{t} + \frac{6m_i}{t^2} \quad (\text{C.2})$$

where  $t$  is the plate thickness.

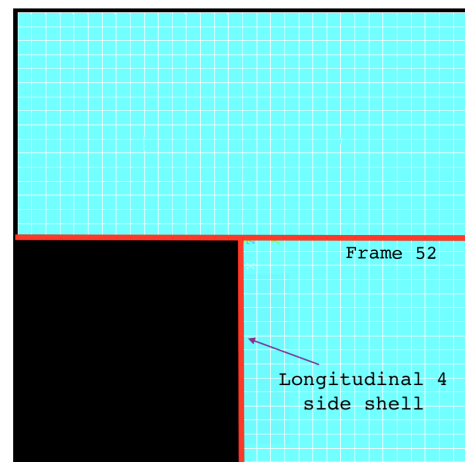
### FE model

An isometric and top view of the FE model is depicted in Figure C.1. Assumptions regarding the dimension were necessary since information on the plate thicknesses was unavailable. The side shell (longitudinal 4) and base plate were assumed to have equal thickness; the frame 52 thickness was assumed to be 80% of the base plate thickness. To mimic the structural response of a ship in waves, displacements were imposed (instead of pressures). The FE model is made using a Shell63 element [1]. The importance of the boundary conditions is recognized. However, the response of the surrounding ship structure is unknown and not all details present in the ship design are modeled in the FE model. It requires more research to determine which boundary conditions are realistic. Boundary conditions that add the least amount of stiffness are assumed. The element size was chosen such that the hot spot stress had converged, but not smaller than the base plate thickness.

Figure C.1a provides a slightly simplistic view to make it more understandable. For example, the heights of frame 52 and longitudinal 4 are reduced in the figure.



(a) Isometric view.



(b) Top view.

Figure C.1: Specification of the FE model.



# D

## Results

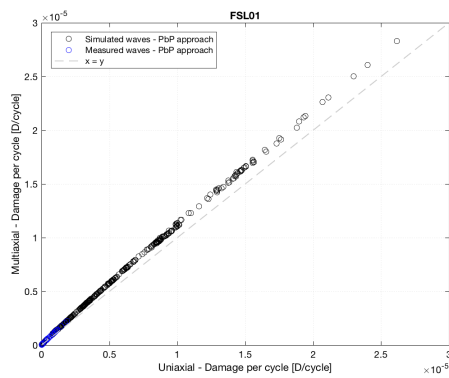


Figure D.1: Uniaxial damage (per cycle) vs. multiaxial damage (per cycle) for FSL01 (TF based).

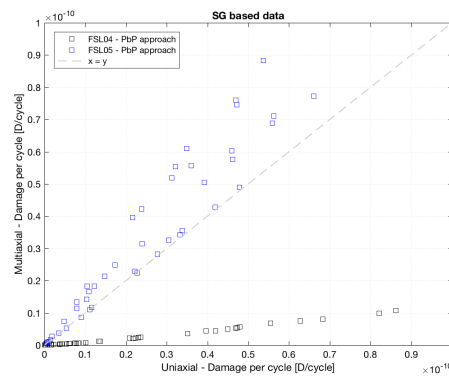


Figure D.2: Uniaxial damage (per cycle) vs. multiaxial damage (per cycle) for FSL04 and FSL05 (strain gauge based).

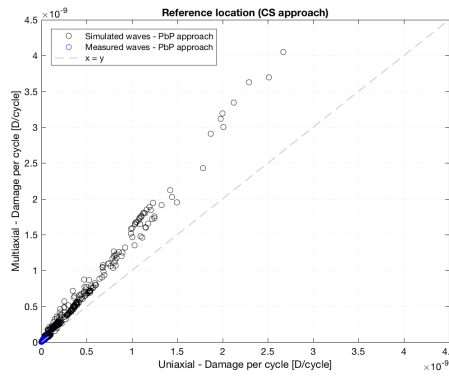


Figure D.3: Uniaxial damage (per cycle) vs. multiaxial damage (per cycle) for the reference location using a cold spot approach (TF damage based).

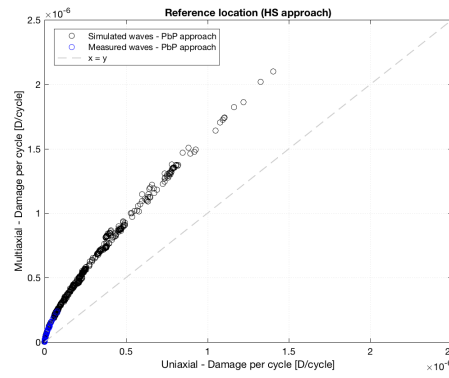
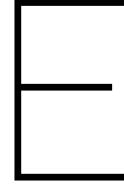


Figure D.4: Uniaxial damage (per cycle) vs. multiaxial (per cycle) for the reference location using a hot spot approach (TF based).

The damage estimates expressed in damage per cycle are depicted in Figures D.1 - D.4. Note that  $D/cycle = 5 \cdot 10^{-7}$  equals an estimated number of cycles to failure of  $N_f = 2 \cdot 10^6$ . Only the data obtained from the PbP approach is included.





# Validation of the Bertholf FE model

To assess the validity of the damage estimates obtained using the FE model, the calculations are compared to the data obtained with the strain gauges. It is preferred to use cold spots for the validation as local influences such as stress concentrations and local stress distributions (V-shaped notch stress) are not taken into account in the FE model. The validation is based on response spectra, meaning that the transfer functions obtained using the FE model cannot be directly related to the measured strains. Detailed wave spectra are necessary to perform the validation. Multiplying the transfer function squared with the wave spectrum (taking into account the heading) results in a 3-D response spectrum; integrating this response spectrum over the wave directions yields the 2-D response spectrum.

The validity of the transfer functions is limited to the validity of the theory (i.e.: potential theory) employed to model the flow around the vessel. It is recommended to perform the validation for a discrete set of vessel speeds, starting at  $v = 0\text{ m/s}$  and working up to the maximum expected sailing speed of the vessel. The transfer function wave direction density depends on the wave direction and the derivative of the transfer functions with respect to the wave direction, and should be investigated.

The validation process consists of two parts:

- Statistical comparison of spectra.
- Quantitative comparison of multiaxial fatigue damage.

## *Statistical comparison*

In the statistical comparison, differences in spectral moments are analyzed. The 2-D response spectrum from the strain gauge measurements is obtained using a Fast Fourier Transform. Spectral moments are defined as:

$$m_n = \int_{-\infty}^{\infty} f^n \cdot S_f(f) dt \quad (\text{E.1})$$

Although some spectral moments represent physical properties (for example: significant wave height, zero up crossing frequency), the physical meaning becomes inconsequential in the comparison of spectra. The comparison should include spectral moments with  $n = 0$ ,  $n < 0$  and  $n > 0$ . Spectral moments with  $n < 0$  give more weight to lower frequencies, Spectral moments with  $n > 0$  give more weight to higher frequencies. A spectral statistical difference (SSD) as defined as:

$$e_n = \frac{(m_{n,E} - m_{n,m})}{m_{n,E}} \quad (\text{E.2})$$

with  $m_{n,e}$  the spectral moment calculated from the FE model data and  $m_{n,m}$  the spectral moment obtained from the strain gauge data. Correlation coefficients are used to quantify comparison between sets of spectral moments and parameters:

- Significant wave height.
- Peak incoming wave direction.

Table E.1: Sets of spectral moments for FE model validation.

Set #	Description
01a	Sum of all SSDs for all stress components.
01b	Sum of SSDs per stress component (both FSLs).
02	One SSD per stress component (both FSLs).

- Spreading.
- Vessel Speed.

The sets of spectral moments are described in Table E.1. Remember that a spectrum is available for every stress component and an SSD is available for every  $n$  (Equation E.1).

Set number 01a is defined to investigate whether all stress components show the same behavior. Set number 01b is defined to find which stress components show the highest errors; whether this is necessary follows from set number 01a. Set number 02 is defined to investigate whether the error is dependent of the loading frequency.

Based on the results, a correction can be defined. For example, it may be so that the error  $e_{-1}$  grows with the vessel speed. This means that lower frequencies are being progressively underestimated with the vessel speed. A correction can now be applied to lower frequencies that depends on the wave height. Another example may be that beam waves overestimate  $m_0$  for stress in  $x$ -direction, which means that the response is overestimated. A correction factor for all frequencies can then be applied.

#### *Quantitative comparison*

Two fatigue methods should be used for the qualitative comparison of multiaxial fatigue damage: the (modified) Projection-by-Projection approach and IIW design rules. The fatigue damage as calculated from the strain gauge measurements creates a benchmark for the fatigue damage percentage error. A number of realizations should be obtained from the 2-D response spectrum with each realization a unique random wave phase, the number of realizations depending on the convergence of the probability spectrum. The expected value of the fatigue damage calculated from the response spectra should be compared to the fatigue damage as obtained from the strain gauge measurements (benchmark value) to obtain the fatigue damage percentage error. The precision can be tested with the realizations made from the response spectrum. The IIW design rules provide a benchmark precision and a benchmark percentage error. The accuracy of the methods cannot be tested since there is no reference value.